

The gravitational force field of proto-pancakes

Shohei Saga^{1,2,3,4}, Stéphane Colombi³, and Atsushi Taruya^{5,6}

¹ Institute for Advanced Research, Nagoya University, Furo-cho Chikusa-ku, Nagoya 464-8601, Japan

² Kobayashi-Maskawa Institute for the Origin of Particles and the Universe, Nagoya University, Chikusa-ku, Nagoya, 464-8602, Japan

³ Sorbonne Université, CNRS, UMR7095, Institut d'Astrophysique de Paris, 98bis boulevard Arago, F-75014 Paris, France

⁴ Laboratoire Univers et Théories, Observatoire de Paris, Université PSL, Université de Paris, CNRS, F-92190 Meudon, France

⁵ Center for Gravitational Physics and Quantum Information, Yukawa Institute for Theoretical Physics, Kyoto University, Kyoto 606-8502, Japan

⁶ Kavli Institute for the Physics and Mathematics of the Universe (WPI), Todai institute for Advanced Study, University of Tokyo, Kashiwa, Chiba 277-8568, Japan

Received –; accepted –

ABSTRACT

It is well known that the first structures that form from small fluctuations in a self-gravitating, collisionless and initially smooth cold dark matter (CDM) fluid are pancakes. We study the gravitational force generated by such pancakes just after shell-crossing, and find a simple analytical formula for the force along the collapse direction, which can be applied to both the single- and multi-stream regimes. The formula is tested on the early growth of CDM protohaloes seeded by two or three crossed sine waves. Adopting the high-order Lagrangian perturbation theory (LPT) solution as a proxy for the dynamics, we confirm that our analytical prediction agrees well with the exact solution computed by direct resolution of the Poisson equation, as long as the caustic structure remains locally sufficiently one-dimensional. These results are further confirmed by comparisons of the LPT predictions performed this way to measurements in Vlasov simulations performed with the public code CoLDICE. We also show that the component of the force orthogonal to the collapse direction preserves its single stream nature by not changing qualitatively before and after the collapse, allowing sufficiently high-order LPT acceleration to be used to approximate it accurately as long as the LPT series converges. As expected, solving Poisson equation on the density field generated with LPT displacement provides a more accurate force than the LPT acceleration itself, as a direct consequence of the faster convergence of the LPT series for the positions than for the accelerations. This may provide a clue on improving standard LPT predictions. Our investigations represent a very needed first step to study analytically gravitational dynamics in the multi-stream regime, by estimating, at leading order in time and space the proper backreaction on the gravitational field inside the pancakes.

Key words. gravitation - galaxies: kinematics and dynamics - dark matter

1. Introduction

Cold dark matter (CDM) is widely admitted to dominate the matter content of the Universe and is microscopically modelled as a self-gravitating collisionless fluid obeying the Vlasov-Poisson equations (Peebles 1982, 1984; Blumenthal et al. 1984). Due to its initially virtually null local velocity dispersion, the CDM phase-space distribution function can be described as a three-dimensional sheet evolving in six-dimensional phase-space. This sheet originally represents a single-stream flow, but as a consequence of the evolution under self-gravity, it can at some point self-intersect in configuration space. Such shell crossings mark the formation of singularities of various kinds, in particular pancake like structures accompanied by apparent divergences of the density field (see, e.g., Zel'dovich 1970; Arnold et al. 1982; Shandarin & Zeldovich 1989; Gouda & Nakamura 1988; Melott & Shandarin 1989; Hidding et al. 2014; Feldbrugge et al. 2018). After the first shell crossings, the sheet repeatedly self-interacts and folds to form intricate multi-stream structures, that include filaments and dark matter haloes. Although numerical simulations have revealed a number of details on the dynamical history of dark matter, it is still difficult to develop an analytical theory capable of predicting the entire growth history of these structures in a fully self-consistent way, due to the highly non-

linear processes involved in multi-stream dynamics. As justified further below, an accurate description of the early stages of the evolution of multistream regions is fundamental to understand these processes and this must go through the calculation of the gravitational force field sourced by pancakes, which is the object of this article.

To approximate dark matter dynamics at large scale one usually relies on perturbation theory (hereafter, PT, see e.g., Bernardeau et al. 2002, for a review). PT has been widely used to predict, in the weakly nonlinear regime, large scale structure statistics such as the power-spectrum and higher order correlation. Many techniques have been developed in this framework (e.g., Crocce & Scoccimarro 2006; Valageas 2007; Crocce & Scoccimarro 2008; Taruya & Hiramatsu 2008; Matsubara 2008; Bernardeau et al. 2008; Pietroni 2008; Taruya et al. 2009; Matsubara 2011; Bernardeau et al. 2012, 2014; Taruya et al. 2012; Valageas et al. 2013) and have been applied to observational data in order to constrain cosmological models (e.g., Blake et al. 2011; Beutler et al. 2017; Zhao et al. 2019; Ivanov et al. 2020; Tröster et al. 2020). In standard PT, a single stream flow is imposed, and the small parameter is the Eulerian density contrast. However, the single-stream approximation is valid only during the early phases of structure formation and its relevance

can be questioned in the PT formalism (see, e.g. Bernardeau et al. 2014; Blas et al. 2014; Nishimichi et al. 2016; Halle et al. 2020). Beyond the single-stream approximation, it is challenging to incorporate backreactions from the multi-stream regions into the analytical predictions in generic situations (see e.g., Rampf 2021, for a recent review). A way to account for multi-streaming on large-scale structure statistics consists in using effective field theory (Baumann et al. 2012; Carrasco et al. 2012; Hertzberg 2014; Baldauf et al. 2015). While effective field theory can provide for practical application meaningful constraints on cosmological models from observational data (e.g., Ivanov et al. 2020; d’Amico et al. 2020), it involves free parameters that need to be calibrated with N -body simulations. For more rigorous treatment beyond phenomenological approach, one solid approach would be to consider high order velocity moments of Vlasov equations accounting for multistreaming. Recently, Garny et al. (2023a,b) succeeded to make the problem analytically tractable, facilitating greatly convergence of PT predictions. However, the approach developed by these authors still depends on simplifying assumptions and there is still room for improvement. Incorporating accurately multi-stream effects into statistical predictions of large-scale structure is thus now considered an important piece for properly extracting cosmological information from observations.

While pancakes generally correspond to the first stages of multistream evolution, filaments and then dark matter haloes represent the next ones, when shell-crossing happens subsequently along transverse directions of motion. The importance of accounting for multi-stream flows has therefore also been recognised in the formation process of protohaloes that allegedly develop monolithically during an early violent relaxation phase (Lynden-Bell 1967) and subsequently, in the CDM scenario, merge hierarchically to form larger haloes with a universal density profile (Navarro et al. 1996, 1997). Although numerical investigations have revealed important properties of protohaloes, e.g., their power-law density profile, $\rho(r) \sim r^{-\alpha}$, with a logarithmic slope $\alpha \approx 1.5$ (Moutarde et al. 1991; Diemand et al. 2005; Ishiyama 2014; Angulo et al. 2017; Ogiya & Hahn 2018; Delos et al. 2018a,b; Colombi 2021; Delos & White 2022; White 2022; Delos & White 2023), there is no exact analytical theory accounting for multi-stream dynamics inside dark matter haloes, despite the multiple approaches to the problem, for instance, self-similarity (Fillmore & Goldreich 1984; Bertschinger 1985; Henriksen & Widrow 1995; Sikivie et al. 1997; Yano & Gouda 1998; Yano et al. 2004; Zuck & Bertschinger 2010b,a; Alard 2013) or entropy maximisation (Lynden-Bell 1967; Hjorth & Williams 2010; Carron & Szapudi 2013; Pontzen & Governato 2013).

One way to push the dynamics beyond shell crossing while preserving total mass conservation consists in using a Lagrangian approach that follows the motion of matter elements as functions of their initial position. Lagrangian PT (LPT), where the displacement field is the small parameter, has been widely employed to accurately describe the large-scale matter distribution in the quasi-linear regime, even beyond shell-crossing (e.g., Zel’dovich 1970; Shandarin & Zeldovich 1989; Bouchet et al. 1992; Buchert 1992; Buchert & Ehlers 1993; Bouchet et al. 1995; Bernardeau 1994). Unfortunately, LPT becomes quickly inaccurate after shell-crossing because it does not account correctly of the force feedback inside multistream regions. Recently some progress has been achieved in this regard in the one-dimensional (1D) case, which corresponds to the simplest dynamical set-up, that is the pure pancake that reduces to the interaction between infinite parallel planes. In 1D, linear LPT

is exact prior to shell-crossing (Novikov 1969), but subsequent multistream evolution still does not have a fully general analytical solution. However, it is possible to derive some approximate solutions asymptotically exact just after shell-crossing, based on LPT but extended beyond collapse and taking into account correctly the backreaction of the gravitational force inside the multi-stream region (Colombi 2015; Taruya & Colombi 2017; Rampf et al. 2021). This article aims to generalize this post-collapse PT approach to three-dimension by calculating the gravitational force in protopanckes with the idea of developing a general analytical treatment of the early stages of multi-stream motion in the general case.

Contrary to the 1D case, one of the difficulties in developing a 3D post-collapse theory is the absence of an exact solution even before shell-crossing. This solution can be approached using sufficiently high order LPT, but as the system approaches the first shell crossing, the perturbative treatment worsens and its convergence speed decreases (e.g., Zeligovsky & Frisch 2014; Rampf et al. 2015; Rampf & Hahn 2021; Rampf et al. 2022, for works on the convergence radius). Convergence speed depends strongly on the nature of initial conditions. It is facilitated when approaching quasi-1D initial conditions (e.g., Rampf & Frisch 2017; Saga et al. 2018) and is made more difficult when approaching axisymmetric configurations or spherical symmetry (e.g., Saga et al. 2018; Rampf 2019). In the simplified approach considered in the present work, we focus on pancakes seeded by a locally symmetric displacement field, a restrictive but still quite generic set up that applies for instance to high peaks of a Gaussian random field (Bardeen et al. 1986). To test our analytical predictions, we consider systems evolving from crossed sine waves initial conditions, that we already studied at collapse in Saga et al. (2018) and slightly beyond shell-crossing in Saga et al. (2022, hereafter, STC). For these systems, we found that LPT is able, at sufficiently high order, to provide an accurate description of the density distribution around shell-crossing so they represent a good ground for testing our analytical predictions for the gravitational force field.

This paper is organised as follows. In Sect. 2, we introduce the basic equations of motion in the Lagrangian description and the LPT framework. We also discuss important aspects of the gravitational force calculation. In Sect. 3, we provide a simple analytical formula for the force inside a pancake in the case the caustic structure is seeded by a locally symmetric displacement. In Sect. 4, our analytical predictions are tested in systems with sine-waves initial conditions, using high order LPT as a proxy for the dynamics. The approximation of the force field is compared to the exact solution of Poisson equation where the density field is generated by the LPT motion. This is followed in Sect. 5 by comparisons of the analytical predictions to the force field directly measured in Vlasov-Poisson simulations performed with the public code ColDICE (Sousbie & Colombi 2016). Finally, Sect. 6 is devoted to the summary of important findings. To supplement the main text, Appendices A, B, and C, respectively test the validity of the series expansion at third order of the displacement field used in Sect. 3, the accuracy of our Green function approach used to compute the force in the theoretical calculations and finally the method we use to measure the force field in the ColDICE simulations.

2. Basic equations and gravitational force

We now introduce the basic equations in the Lagrangian description (Sect. 2.1) and discuss important aspects of the gravitational force calculation in the framework of LPT (Sect. 2.2).

2.1. Lagrangian dynamical framework

We consider the Lagrangian equation of motion of a fluid element at the Eulerian comoving position \mathbf{x} in the presence of gravity (e.g., Peebles 1980):

$$\frac{d^2\mathbf{x}}{dt^2} + 2H\frac{d\mathbf{x}}{dt} = -\frac{1}{a^2}\nabla_{\mathbf{x}}\phi(\mathbf{x}), \quad (1)$$

where the quantities a , $H(t) = a^{-1}da/dt$, and $\phi(\mathbf{x})$ are the scale factor of the Universe, the Hubble parameter, and the Newton gravitational potential, respectively, and the operator $\nabla_{\mathbf{x}} = \partial/\partial\mathbf{x}$ is the spatial gradient in Eulerian space. The gravitational potential is related to the matter density contrast $\delta(\mathbf{x}) = \rho(\mathbf{x})/\bar{\rho} - 1$ with $\bar{\rho}$ the background mass density, through the Poisson equation:

$$\nabla_{\mathbf{x}}^2\phi(\mathbf{x}) = 4\pi G a^2 \bar{\rho} \delta(\mathbf{x}). \quad (2)$$

The Lagrangian description relates the initial, Lagrangian position, \mathbf{q} , of each mass element to the Eulerian position at time t , $\mathbf{x}(\mathbf{q}, t)$, through the introduction of the displacement field, $\Psi(\mathbf{q}, t)$. In this framework, the Eulerian position \mathbf{x} and velocity \mathbf{v} are given by

$$\mathbf{x}(\mathbf{q}, t) = \mathbf{q} + \Psi(\mathbf{q}, t), \quad (3)$$

$$\mathbf{v} = a \frac{d\Psi}{dt}. \quad (4)$$

Assuming homogeneous initial density, $\rho(\mathbf{q})/\bar{\rho} = 1$, mass conservation reads $d^3\mathbf{q} = (1 + \delta(\mathbf{x})) d^3\mathbf{x}$ before the first shell-crossing time t_{sc} . Hence,

$$1 + \delta(\mathbf{x}) = \frac{1}{J}, \quad (5)$$

where the quantity $J = \det J_{ij}$ is the Jacobian of the matrix J_{ij} defined by

$$J_{ij}(\mathbf{q}, t) = \frac{\partial x_i(\mathbf{q}, t)}{\partial q_j} = \delta_{ij} + \Psi_{i,j}(\mathbf{q}, t). \quad (6)$$

The first occurrence of $J = 0$ determines the first shell-crossing time t_{sc} .

Until the first shell-crossing, we can employ a perturbative treatment to predict the fluid motion, namely Lagrangian perturbation theory (LPT, e.g., Zel'dovich 1970; Shandarin & Zel'dovich 1989; Bouchet et al. 1992; Buchert 1992; Buchert & Ehlers 1993; Bouchet et al. 1995; Bernardeau 1994). In LPT, the displacement field, Ψ , is considered a small quantity, which is systematically expanded as

$$\Psi(\mathbf{q}, t) = \sum_{n=1}^{\infty} \Psi^{(n)}(\mathbf{q}, t). \quad (7)$$

Assuming that the fastest growing modes dominate, the perturbative solution is approximated quite well by the form (see, e.g., Bernardeau et al. 2002, and references therein):

$$\Psi^{(n)}(\mathbf{q}, t) = D_+(t) \Psi^{(n)}(\mathbf{q}), \quad (8)$$

with the time-dependent function $D_+(t)$ being the linear growth factor. Substituting Eq. (8) into Eq. (4), the velocity field is given by

$$\mathbf{v}(\mathbf{q}, t) = a H f \sum_{n=1}^{\infty} n D_+^n(t) \Psi^{(n)}(\mathbf{q}), \quad (9)$$

where we define the linear growth rate by $f(t) \equiv d \ln D_+ / d \ln a$.

In equations (8) and (9) the n^{th} order displacement $\Psi^{(n)}$ is computed recursively by exploiting equations (1) and (2) using well known algebraic techniques (see, e.g. Rampf 2012; Zheigovsky & Frisch 2014; Rampf et al. 2015; Matsubara 2015). Specific expressions for the three sine wave case examined below are given in STC and we do not consider it necessary to recall them. The Lagrangian framework we are using in this article relies in practice on perturbation theory as a proxy of the dynamics. However the analytic expressions computed in Sect. 3 are more general in the sense that they apply (asymptotically, that is just beyond shell-crossing) to any non-degenerate displacement field locally symmetric and Taylor expandable up to third order in the Lagrangian position around the singularity of interest.

2.2. Gravitational force

To facilitate resolution of Poisson equation (2), we decompose it into two independent equations:

$$\nabla_{\mathbf{x}}^2\phi_p = 4\pi G \bar{\rho} a^2 (1 + \delta(\mathbf{x})), \quad (10)$$

$$\nabla_{\mathbf{x}}^2\bar{\phi} = -4\pi G \bar{\rho} a^2. \quad (11)$$

Then,

$$\phi(\mathbf{x}) = \phi_p(\mathbf{x}) + \bar{\phi}(\mathbf{x}). \quad (12)$$

The first and second terms of the right-hand side of this equation are respectively the gravitational potential coming from the total density $\bar{\rho}(1 + \delta(\mathbf{x}))$ and the negative background density $-\bar{\rho}$ as counter-term. After solving Eqs. (10) and (11), the gravitational acceleration, also abusively referred to here as force $\mathbf{F}(\mathbf{x}) = -\nabla_{\mathbf{x}}\phi(\mathbf{x})$, is given by

$$\mathbf{F}(\mathbf{x}) = 4\pi G a^2 \bar{\rho} \left(\int \frac{d^d\mathbf{x}'}{2^{d-1}\pi} \frac{(1 + \delta(\mathbf{x}'))(\mathbf{x} - \mathbf{x}')}{|\mathbf{x} - \mathbf{x}'|^n} + \frac{1}{d}\mathbf{x} \right), \quad (13)$$

$$= 4\pi G a^2 \bar{\rho} \left(\int \frac{d^d\mathbf{q}}{2^{d-1}\pi} \frac{\mathbf{x} - \mathbf{x}'(\mathbf{q})}{|\mathbf{x} - \mathbf{x}'(\mathbf{q})|^n} + \frac{1}{d}\mathbf{x} \right), \quad (14)$$

where d represents the dimension of space ($d = 2$ or 3 considered in this paper). In the second line, we used mass conservation in d -dimensional space: $(1 + \delta(\mathbf{x}')) d^d\mathbf{x}' = d^d\mathbf{q}$. The second term in parentheses represents the gravitational force arising from the background density in Eq. (11).

Thanks to the change of variable $\mathbf{x} \rightarrow \mathbf{q}$, the expression of the force in Eq. (14) does not depend explicitly on the density contrast nor does it require a detailed knowledge of the multi-stream structure, which is, regardless of its complexity, implicitly contained in the function $\mathbf{x}(\mathbf{q})$. This considerably facilitates the numerical calculation of the integrals without the need to solve a multivalued problem. Note that this property was exploited before to compute the gravity field from caustic rings (see e.g., Sikivie 1998, 1999; Natarajan & Sikivie 2006, 2007; Duffy & Sikivie 2008; Onemli & Sikivie 2009; Chakrabarty & Sikivie 2018; Tam 2012) and the calculations we perform here are analogous.

While integral (14) seems simpler to estimate than integral (13), because it is performed in Lagrangian space, it remains challenging to compute it analytically and the main goal of the present work is to find explicit expressions approximating it.

Another way to estimate the gravitational acceleration consists in simply computing the second time derivative of the Lagrangian displacement (provided that it is sourced by pure gravity). Consider the presence of n_S streams at Eulerian position \mathbf{x} .

In this case, the acceleration can be formally written as the local average of the time derivatives of velocities over all the streams weighted by the density of each stream:

$$\mathbf{F}(\mathbf{x}) = \frac{\sum_{i=1}^{n_s} \rho_i(\mathbf{x}) \mathbf{\Gamma}_i(\mathbf{x})}{\sum_{i=1}^{n_s} \rho_i(\mathbf{x})}, \quad (15)$$

$$\mathbf{\Gamma}_i(\mathbf{x}) \equiv \frac{d(a \mathbf{v}_i(\mathbf{x}))}{dt}, \quad (16)$$

where the quantities ρ_i and $a \mathbf{v}_i$ stand for the density and peculiar velocity of i^{th} stream, respectively. If one has access to the exact solution of the dynamics, this expression is somewhat trivial since, in this case, $\mathbf{\Gamma}_i(\mathbf{x}) = \mathbf{\Gamma}_j(\mathbf{x})$, $i \neq j$. On the other hand, if the accelerations in Eq. (15) are given by second time derivatives of the LPT displacement computed at some order, the force in Eq. (15) does not generally agree with Eq. (14) applied to the same displacement field, even in the single stream regime. Indeed, the LPT solutions are derived not by directly solving the Poisson equation as in Eq. (14) but by perturbatively solving the Lagrangian equations of motion.

Equation (14), which is strongly nonlinear in essence as it can account accurately of multistreams, acts as a resummation of the LPT acceleration: it is expected to provide a more accurate prediction of the gravitational force field than the second time derivative of the LPT displacement. However, as long as the LPT series converges, we expect the higher-order LPT acceleration to converge to the force given by Eq. (14) in the single stream regime, and this property will turn out to be useful even in the multistream regime when estimating the gravitational force orthogonal to the shell-crossing direction (coplanar with the pancake) by using Eq. (15).

3. Analytical predictions for the gravitational force

In this section, we aim to compute the gravitational force shortly after the first shell-crossing in three-dimensional space. As detailed in Sect. 3.1, we restrict to the formation of a symmetric pancake seeded by a locally axisymmetric motion. The calculation of the component of the force along the shell-crossing direction is the most challenging. However, after Taylor expanding the Lagrangian displacement field around the singularity just after shell-crossing, it turns out to be very similar to the pure one-dimensional case already treated in Gurevich & Zybin (1995); Colombi (2015); Taruya & Colombi (2017); Rampf et al. (2021). In particular it involves the resolution of a three-value problem related to the three flows inside the proto-pancake, as detailed in Sect. 3.2. The expression for the force along the shell-crossing direction is given in Sect. 3.3. In this subsection, we also argue that the force field in the transverse direction should not be significantly affected by the multi-stream nature of the flow, which will allow us to estimate it directly as the second time derivative of the displacement estimated with high-order LPT.

3.1. Main assumptions

In what follows, the calculations are all performed in 3D space, but the extension to 2D is straightforward by ignoring or setting to zero all the contributions depending on z . We also suppose that the first shell-crossing takes place at the origin, $\mathbf{q} = \mathbf{x} = \mathbf{0}$, along the x -axis direction, and also that the system exhibits locally axisymmetric dynamics. This setup, illustrated by Fig. 1, seemingly appears to be very particular, but locally represents the expected motion around high peaks of a Gaussian random field (see e.g., Bardeen et al. 1986).

Axisymmetric dynamics translates as follows on the displacement $\Psi(\mathbf{q})$:

$$\begin{aligned} \Psi_x(q_x, q_y, q_z) &= \Psi_x(q_x, -q_y, q_z) = \Psi_x(q_x, q_y, -q_z) \\ &= -\Psi_x(-q_x, q_y, q_z), \end{aligned} \quad (17)$$

$$\begin{aligned} \Psi_y(q_x, q_y, q_z) &= \Psi_y(q_x, q_y, -q_z) = \Psi_y(-q_x, q_y, q_z) \\ &= -\Psi_y(q_x, -q_y, q_z), \end{aligned} \quad (18)$$

$$\begin{aligned} \Psi_z(q_x, q_y, q_z) &= \Psi_z(-q_x, q_y, q_z) = \Psi_z(q_x, -q_y, q_z) \\ &= -\Psi_z(q_x, q_y, -q_z). \end{aligned} \quad (19)$$

Here and hereafter, we omit the time dependence in the notations. Expanding these functions around the origin $\mathbf{q} = \mathbf{0}$, we have

$$\Psi_x(\mathbf{q}) = \sum_{i,j,k=0} \frac{\psi_{2i+1, 2j, 2k}}{(2i+1)!(2j)!(2k)!} q_x^{2i+1} q_y^{2j} q_z^{2k}, \quad (20)$$

$$\Psi_y(\mathbf{q}) = \sum_{i,j,k=0} \frac{\psi_{2i, 2j+1, 2k}}{(2i)!(2j+1)!(2k)!} q_x^{2i} q_y^{2j+1} q_z^{2k}, \quad (21)$$

$$\Psi_z(\mathbf{q}) = \sum_{i,j,k=0} \frac{\psi_{2i, 2j, 2k+1}}{(2i)!(2j)!(2k+1)!} q_x^{2i} q_y^{2j} q_z^{2k+1}, \quad (22)$$

with ψ_{ijk} being some functions of time. Substituting Eqs. (20)–(22) into Eq. (3), and neglecting $O(q^4)$ and higher order terms, we obtain

$$x(\mathbf{q}) \simeq (1 + \psi_{100}) q_x + \frac{1}{2} (\psi_{120} q_y^2 + \psi_{102} q_z^2) q_x + \frac{1}{6} \psi_{300} q_x^3, \quad (23)$$

$$y(\mathbf{q}) \simeq (1 + \psi_{010}) q_y + \frac{1}{2} (\psi_{012} q_z^2 + \psi_{210} q_x^2) q_y + \frac{1}{6} \psi_{030} q_y^3, \quad (24)$$

$$z(\mathbf{q}) \simeq (1 + \psi_{001}) q_z + \frac{1}{2} (\psi_{201} q_x^2 + \psi_{021} q_y^2) q_z + \frac{1}{6} \psi_{003} q_z^3. \quad (25)$$

While this local representation of the motion is minimal, it remains accurate shortly after collapse as illustrated by Appendix A.

We now write the necessary conditions that the coefficients in Eqs. (23)–(25) must satisfy for a pancake to exist near the origin. It is important to note that these conditions do not necessarily imply that a halo subsequently forms, this would require more restrictive constraints.

Since we consider a system in which first shell-crossing just took place along the x -direction at $\mathbf{q} = \mathbf{0}$, we impose

$$\frac{\partial x(\mathbf{0})}{\partial q_x} \equiv -h = 1 + \psi_{100} < 0, \quad 0 < h \ll 1, \quad (26)$$

$$\frac{\partial y(\mathbf{0})}{\partial q_y} = 1 + \psi_{010} > 0, \quad (27)$$

$$\frac{\partial z(\mathbf{0})}{\partial q_z} = 1 + \psi_{001} > 0. \quad (28)$$

Additional constraints can be obtained from the expression of the Jacobian determinant, $J = \det \partial \mathbf{x} / \partial \mathbf{q}$ at leading order in \mathbf{q} , which reads

$$J \simeq \frac{1}{2} (1 + \psi_{010})(1 + \psi_{001}) (-2h + \psi_{120} q_y^2 + \psi_{102} q_z^2 + \psi_{300} q_x^2). \quad (29)$$

From catastrophe theory (see, e.g., Hidding et al. 2014; Feldbrugge et al. 2018, and references therein), the caustic surface should be an ellipsoid outside of which the Jacobian determinant must have a positive value $J > 0$, so we impose

$$\psi_{120} > 0, \quad \psi_{102} > 0, \quad \psi_{300} > 0. \quad (30)$$

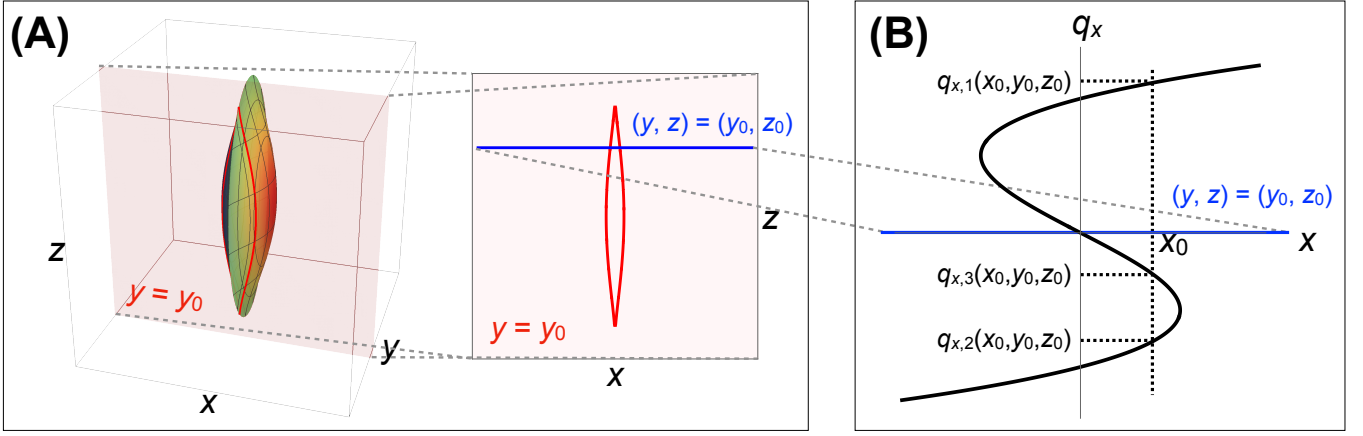


Fig. 1. (A) *Left:* schematic representation of a three-dimensional Eulerian caustics shortly after shell-crossing along x -axis direction, together with a two-dimensional slice with $y = y_0$ (light-red plane). *Right:* the intersection of the caustic surface with the slice (red curve), also shown in the left panel. (B) Schematic representation of the x -component of the Lagrangian coordinate q_x as a function of the Eulerian coordinate x for fixed (y_0, z_0) (solid blue line). Given x_0 , the solution of the three-value problem $x(q_x) = x_0$ is given by $q_{x,n}(x_0, y_0, z_0)$ for $n = 1, 2$, and 3 , as in Eq. (41).

Finally, the smallness of the h parameter induces an additional simplification of Eqs. (23)–(25) if one supposes that Lagrangian coordinates are restricted to lie in the neighbourhood of the pancake, i.e. $q_x \sim q_y \sim q_z \sim O(h^{1/2})$ from Eq. (29). In this case, one realizes that, when examining Eqs. (23)–(25),

$$x(\mathbf{q}) = O(h^{3/2}), \quad (31)$$

$$y(\mathbf{q}) \simeq (1 + \psi_{010})q_y + O(h^{3/2}), \quad (32)$$

$$z(\mathbf{q}) \simeq (1 + \psi_{001})q_z + O(h^{3/2}), \quad (33)$$

which implies $|x| \sim O(h^{3/2}) \ll |y|, |z| \sim O(h^{1/2})$, a signature of the pancake nature of the system: the extension of the caustic region along the x -axis is asymptotically infinitely smaller than that along the other axes in the limit $h \rightarrow 0$, as illustrated by panel (A) of Fig. 1. Accordingly, inside and in the vicinity of the caustic region, we can ignore the higher-order terms in the expressions of y and z , and reduce Eqs. (23)–(25) to

$$x(\mathbf{q}) \simeq (1 + \psi_{100})q_x + \frac{1}{2}(\psi_{120}q_y^2 + \psi_{102}q_z^2)q_x + \frac{1}{6}\psi_{300}q_x^3, \quad (34)$$

$$y(\mathbf{q}) \simeq (1 + \psi_{010})q_y, \quad (35)$$

$$z(\mathbf{q}) \simeq (1 + \psi_{001})q_z. \quad (36)$$

Eqs. (34)–(36) represent our starting point to derive the x -component of the gravitational force inside a pancake.

3.2. The three value problem

Despite its apparent simplicity, Eq. (14) is not easily exploitable when it comes to estimate the gravitational force analytically, even with as simple expressions as Eqs. (34)–(36). Indeed, although the multi-stream nature of the flow does not appear explicitly in the integral (14), we shall see in Sect. 3.3 that the calculation of the x -component of the gravitational force still requires solving the three-valued problem implicit in Eqs. (34)–(36), that is finding \mathbf{q} given \mathbf{x} .

From Eqs. (35) and (36), we trivially obtain

$$q_y = \frac{y}{1 + \psi_{010}}, \quad q_z = \frac{z}{1 + \psi_{001}}. \quad (37)$$

The calculation of $q_x(\mathbf{x})$ is more complex because it requires solving the following cubic equation, as illustrated by panel (B) of Fig. 1,

$$q_x^3 + 3A(y, z)q_x + 2B(x) = 0, \quad (38)$$

where we defined

$$A(y, z) = \frac{1}{\psi_{300}} \left(-2h + \psi_{120} \left(\frac{y}{1 + \psi_{010}} \right)^2 + \psi_{102} \left(\frac{z}{1 + \psi_{001}} \right)^2 \right), \quad (39)$$

$$B(x) = -\frac{3x}{\psi_{300}}. \quad (40)$$

The roots of cubic Eq. (38) are given by (see e.g., Abramowitz & Stegun 1972)

$$q_{x,n}(\mathbf{x}) = \omega^{n-1} \frac{-A(y, z)}{(\sqrt{D(\mathbf{x})} - B(x))^{1/3}} + \omega^{4-n} (\sqrt{D(\mathbf{x})} - B(x))^{1/3}, \quad (41)$$

for $n = 1, 2$, and 3 . Here, the factor ω is one of the complex cubic roots of unity, i.e., $\omega = (-1 \pm i\sqrt{3})/2$, which are the solutions of $\omega^2 + \omega + 1 = 0$. We define the discriminant $D(\mathbf{x})$, which determines the properties of the roots (41), by (e.g., Abramowitz & Stegun 1972)

$$D(\mathbf{x}) = (A(y, z))^3 + (B(x))^2. \quad (42)$$

First note that the equation $D(\mathbf{x}) = 0$ defines the caustics surfaces in Eulerian space:

$$\left[-2h + \psi_{120} \left(\frac{y}{1 + \psi_{010}} \right)^2 + \psi_{102} \left(\frac{z}{1 + \psi_{001}} \right)^2 \right]^3 + 9\psi_{300}x^2 = 0. \quad (43)$$

According to the sign of $D(\mathbf{x})$, the solutions of the cubic equation (38) can then be classified as follows. If $D(\mathbf{x}) < 0$, we are inside the multi-stream region delimited by the caustic surfaces: the cubic equation has three real solutions, with $q_{x,2} < q_{x,3} < q_{x,1}$ and $q_{x,2} < 0 < q_{x,1}$. If $D(\mathbf{x}) > 0$, we are outside the multi-stream region: only either $q_{x,1}$ or $q_{x,2}$ is real, and the other solutions are complex conjugate to each other.

As a final note, from Eq. (43), the maximum values of the Eulerian coordinates of caustics along the x -, y -, and z -axes are given by

$$x_{\max} = \sqrt{\frac{8h^3}{9\psi_{300}}}, \quad (44)$$

$$y_{\max} = (1 + \psi_{010}) \sqrt{\frac{2h}{\psi_{120}}}, \quad (45)$$

$$z_{\max} = (1 + \psi_{001}) \sqrt{\frac{2h}{\psi_{102}}}, \quad (46)$$

Once again, $x_{\max} \ll y_{\max}, z_{\max}$ in the limit $h \rightarrow 0$.

3.3. The Force field inside a pancake

We now present the main results of this paper. Focusing on the dynamics just after the first shell crossing along x -direction, we first derive an analytical formula for the x -component of the gravitational force after collapse. Next, we discuss orthogonal components and argue that they can be directly approximated by the high-order LPT acceleration.

By zooming in very closely on the multi-stream region, we notice that the structure of the density field becomes almost one

dimensional when $h \rightarrow 0$. This follows from the fact the size of the pancake along the x -axis is much smaller than along orthogonal directions (see Eqs. 31–33 and also panel A of Fig. 1). Consequently, given the Eulerian position (x, y_0, z_0) for y_0 and z_0 fixed, solving the Poisson equation (10) is asymptotically reduced to a one-dimensional problem along x axis, as schematically shown in panel (B) of Fig. 1. In this case, we can neglect local variations of the density along the y and z -directions, and Eq. (10) reduces to the following one-dimensional Poisson equation for the x -coordinate of the gravitational acceleration,

$$\begin{aligned} \frac{d^2 \phi_p(x, y_0, z_0)}{dx^2} &= 4\pi G \bar{\rho} a^2 (1 + \delta(x, y_0, z_0)), \\ &= 4\pi G \bar{\rho} a^2 \frac{1}{(1 + \psi_{010})(1 + \psi_{001})} \left| \frac{\partial x}{\partial q_x} \right|^{-1}, \end{aligned} \quad (47)$$

where, in the second equality, we have used Eq. (5) with Eqs. (34)–(36).

To solve this equation, we follow the footsteps of Colombi (2015); Taruya & Colombi (2017); Rampf et al. (2021) and employ a Green function approach to derive the x -component of the force in the multi-stream region, $F_x(\mathbf{x}_0) \simeq -d\phi_p(\mathbf{x}_0)/dx$ with $\mathbf{x}_0 = (x_0, y_0, z_0)$ (inside the pancake, $x \sim h^{3/2}$, and the background contribution $\bar{\phi}$ is negligible):

$$\begin{aligned} F_x(\mathbf{x}_0) &\simeq \int dx \frac{4\pi G \bar{\rho} a^2}{(1 + \psi_{010})(1 + \psi_{001})} \sum_{n=0,1,2} \left| \frac{\partial x}{\partial q_{x,n}} \right|^{-1} \frac{1}{2} [\Theta_H(x - x_0) - \Theta_H(x_0 - x)], \\ &= \int dq_x \frac{4\pi G \bar{\rho} a^2}{(1 + \psi_{010})(1 + \psi_{001})} \frac{1}{2} \left[\Theta_H \left(x \left(q_x, \frac{y_0}{1 + \psi_{010}}, \frac{z_0}{1 + \psi_{001}} \right) - x_0 \right) - \Theta_H \left(x_0 - x \left(q_x, \frac{y_0}{1 + \psi_{010}}, \frac{z_0}{1 + \psi_{001}} \right) \right) \right], \\ &= -\frac{4\pi G \bar{\rho} a^2}{(1 + \psi_{010})(1 + \psi_{001})} [q_{x,1}(\mathbf{x}_0) + q_{x,2}(\mathbf{x}_0) - q_{x,3}(\mathbf{x}_0)] \quad (\text{in the multi-stream region}), \end{aligned} \quad (48)$$

where Θ_H represents the Heaviside step function, and the quantities $q_{x,n}$ are the three-value problem solutions given in Eq. (41). In the first line of Eq. (48), we have dropped the negligible contributions in the one-dimensional Green function that are not proportional to the Heaviside step function.

Interestingly, one can also write, asymptotically,

$$F_x(\mathbf{x}_0) \simeq \Gamma_x[q_{x,1}(\mathbf{x}_0)] + \Gamma_x[q_{x,2}(\mathbf{x}_0)] - \Gamma_x[q_{x,3}(\mathbf{x}_0)], \quad (49)$$

where Γ_x , defined in Eq. (16), is the x -coordinate of the LPT acceleration (computed by ignoring shell-crossing). This approximation will be tested in Sect. 5.

Eq. (48) applies only to the multi-stream region. However, as mentioned above, in the single-stream region, either $q_{x,1}$ or $q_{x,2}$ is real while the two other values are complex conjugate to each other. Taking the real part of right hand side of Eq. (48), the unphysical contribution arising from the complex conjugate solutions vanishes, leaving only the physical contribution from

one real solution¹:

$$F_x(\mathbf{x}_0) \simeq -\frac{4\pi G \bar{\rho} a^2}{(1 + \psi_{010})(1 + \psi_{001})} \text{Re} [q_{x,1}(\mathbf{x}_0) + q_{x,2}(\mathbf{x}_0) - q_{x,3}(\mathbf{x}_0)]. \quad (51)$$

Here, “Re” denotes the real part.

Eq. (51) is the most important formula in our work. Together with the solution of the cubic equation (41), it consists of a simple algebraic form for the x -component of the force in the vicinity of the pancake, inside and outside it. This formula is the natural extension to three dimensions of the one dimensional calculations of Gurevich & Zybin (1995); Colombi (2015); Taruya & Colombi (2017); Rampf et al. (2021).

The components F_y and F_z of the force orthogonal to the shell-crossing direction, hence coplanar with the pancake, should, on the other hand, remain quite insensitive to the effects of shell-crossing, as we will show with the numerical tests performed in next sections. This means that if the LPT displacement

¹ Equivalently, we can rewrite Eq. (48) as follows:

$$F_x(\mathbf{x}_0) = -\frac{4\pi G \bar{\rho} a^2}{(1 + \psi_{010})(1 + \psi_{001})} [q_{x,1}(\mathbf{x}_0) + q_{x,2}(\mathbf{x}_0) - (q_{x,3}(\mathbf{x}_0))^*] \quad (50)$$

where the asterisk denotes the complex conjugate.

field is entirely sourced by gravity, its second time derivative should provide a very good approximation of the local gravitational acceleration, even slightly beyond shell crossing. As a consequence, the acceleration directly derived from the high-order LPT solution (with no Taylor expansion at third order in \mathbf{q} space) should provide a good approximation for F_y and F_z . Of course this is true only if one remains within the convergence radius of the LPT series, which is finite in the general case (e.g., Zeligovsky & Frisch 2014; Rampf et al. 2015; Rampf & Hahn 2021). To overcome the three-value problem, the acceleration can be obtained with the weighted average (15) over the different flows inside the pancake, even though this is not absolutely necessary, since it is expected, in the vicinity of the pancake, that $F_y[\mathbf{x}(\mathbf{q}_1)] \simeq F_y[\mathbf{x}(\mathbf{q}_2)] \simeq F_y[\mathbf{x}(\mathbf{q}_3)]$ and similarly for the z -component of the force: this is due to the fact that the vectors \mathbf{q}_1 , \mathbf{q}_2 and \mathbf{q}_3 are nearly equal.

4. Examination of the accuracy of the formulas

In this section, we test the validity and the accuracy of our prescription for calculating the post-collapse force. To this end, we assume Einstein-de Sitter cosmology and consider simplified initial conditions composed of two or three crossed sine waves, following the early investigations of Moutarde et al. (1991, 1995) and our previous works (Saga et al. 2018). We present these initial conditions in Sect. 4.1, where we also give practical details on the way the analyses are performed. Sect. 4.2 focuses on the force along the shell-crossing direction. We test, at different orders of the perturbative development, the accuracy of Eq. (51) against the exact solution obtained by direct resolution of Poisson equation. This is followed in Sect. 4.3 by a comparison, in the transverse direction, of the LPT acceleration to the exact force. All these analyses are performed very shortly after collapse to make sure that assumptions of Sect. 3.1 are verified. One indeed expects increasing discrepancies with time between the exact solution and the approximations of the dynamics, as examined in Sect. 4.4.

Throughout this section, we use the LPT solution as a proxy for the “exact” Eulerian position. To calculate the “exact” force field, we simply inject the LPT solution into Eq. (14) and numerically perform the two- or three-dimensional integrals.² The comparisons to simulations performed in Sect. 5 will show that this proxy turns to provide a quite accurate description of the true displacements at the times we consider.

4.1. Two and three sine waves initial conditions: practical implementation

We consider initial conditions seeded by two or three crossed sine waves in a periodic box $[-L/2, L/2[$ in which the initial displacement field at initial time t_{ini} is expressed by (see STC)

$$\Psi_i^{\text{ini}}(\mathbf{q}, t_{\text{ini}}) = \frac{L}{2\pi} D_+(t_{\text{ini}}) \epsilon_i \sin\left(\frac{2\pi}{L} q_i\right), \quad (52)$$

with $\epsilon_i < 0$ and $|\epsilon_x| \geq |\epsilon_y| \geq |\epsilon_z|$. The initial density field, $\delta^{\text{ini}} \simeq -\nabla_{\mathbf{q}} \cdot \Psi^{\text{ini}} = D_+(t_{\text{ini}}) \sum_i |\epsilon_i| \cos(2\pi/L q_i)$, presents a small peak

² In numerically integrating Eq. (14), we use the `NIntegrate` function in `Mathematica` with the options `{MaxRecursion -> 100 (10000), PrecisionGoal -> 5 (8), Method -> {Automatic, "SymbolicProcessing" -> 0}}` for F_x ($F_{y,z}$). In this instance, the computation of the results depicted in Figs. 2 or 3, on an 8-core CPU laptop, takes several hours.

at the origin. Subsequently, mass elements fall towards the overdense central region, and shell-crossing takes place at the origin. The initial time, t_{ini} , is set to satisfy $D_+(t_{\text{ini}})|\epsilon_i| \leq 0.012 \ll 1$, so that the fastest growing mode approximation is accurate (Saga et al. 2018). We note that in the Einstein-de Sitter universe, the growth factor is simply proportional to the scale factor and we have $f = 1$. Hence, we shall hereafter use the scale factor to describe the time rather than D_+ .

In this setup, the dynamics is determined by the ratios $\epsilon_{2D} = \epsilon_y/\epsilon_x$ and $\epsilon_{3D} = (\epsilon_y/\epsilon_x, \epsilon_z/\epsilon_x)$, respectively for two and three sine waves initial conditions (STC). We consider three qualitatively different initial conditions as detailed in Table 1: quasi one-dimensional with $|\epsilon_x| \gg |\epsilon_{y,z}|$ (Q1D), anisotropic with $|\epsilon_x| > |\epsilon_y| > |\epsilon_z|$ (ANI), and axial-symmetric with $|\epsilon_x| = |\epsilon_y| = |\epsilon_z|$ (SYM). The Q1D and ANI initial conditions are the primary targets of our analyses because first shell crossing occurs only along the x -direction, satisfying the assumptions of Sect. 3.1. On the other hand, for the SYM case, since shell crossing takes place simultaneously along two or three axial directions, the prescriptions proposed in Sect. 3.3 to approximate the force field becomes improper. However, the SYM case might provide insight into rare primordial haloes and remains mathematically interesting. In this case, we will only explore numerically in Sect. 5 the force field by comparing predictions of higher-order LPT combined with the Green function approach (Eq. 14) to measurements in the simulations.

Sine waves initial conditions (52) correspond to a low order trigonometric polynomial, which makes LPT calculations relatively cheap and allows us to reach 40th and 15th order for the two- and three-dimensional case, respectively (see Sect. 2 in STC for the explicit procedure).³

Having obtained the higher-order LPT solutions, we analytically predict the force along the shell-crossing direction using Eq. (51), by expanding the LPT solutions around the origin up to third order in terms of Lagrangian coordinates to have the expressions for the coefficients ψ_{ijk} in Eqs. (20)–(22) hence in formula (51). Also, we analytically predict the force orthogonal to the shell-crossing direction by directly using the LPT acceleration (without Taylor expanding it in \mathbf{q}) and averaging it (numerically) over different flows at same Eulerian position \mathbf{x} using Eq. (15).

Because the collapse time, traced here by the value of the expansion factor $a_{\text{sc}}^{(n)}$, decreases when perturbative order n augments (see, e.g., STC), LPT predictions are in practice synchronized to their own respective shell-crossing times. Then the system is evolved beyond collapse by a very small amount of time, i.e.,

$$a^{(n)} = a_{\text{sc}}^{(n)} (1 + \Delta), \quad (53)$$

where Δ is a small parameter, such that the assumptions of Sect. 3.1 are valid, in particular $h \simeq \Delta |\partial v_x / \partial q_x| / (aH)|_{q=0, t=t_{\text{sc}}} \ll 1$. In practice, we shall take $\Delta = 0.001$ in Secs. 4.2 and 4.3, while it will be allowed to be larger in Sect. 4.4.

As a final note, we truncate the integral in Eq. (14) to a finite interval $[-q_{\text{max}}, q_{\text{max}}]$ in each dimension, setting $q_{\text{max}} = L/2$ for F_x and $q_{\text{max}} = 10L$ for $F_{y,z}$ to insure convergence of the integral, as studied in Appendix B.

In the rest of the paper, we will use the following units: a box size $L = 1$ and an inverse of the Hubble parameter at the present time $H_0 = 1$ for the dimensions of length and time, respectively.

³ The high-order LPT solutions can be provided upon request as a `Mathematica` notebook.

Designation	ϵ_{2D} or ϵ_{3D}	ϵ_x	n_g	n_s	a_{sc}^{LPT}	a_{sc}	a_{sim}	$\Delta_{sim} \equiv (a_{sim} - a_{sc})/a_{sc}$
<i>Quasi 1D</i>								
Q1D-2SIN	1/6	-18	2048	2048	0.05279	0.05285	0.05402	0.02219
Q1D-3SIN	(1/6, 1/8)	-24	512	256	0.03814	0.03832	0.03907	0.01974
<i>Anisotropic</i>								
ANI-2SIN	2/3	-18	2048	2048	0.04534	0.04545	0.04601	0.01230
ANI-3SIN	(3/4, 1/2)	-24	512	512	0.02912	0.02919	0.03003	0.02890
<i>Axial-symmetric</i>								
SYM-2SIN	1	-18	2048	2048	0.04087	0.04090	0.04101	0.002717
SYM-3SIN	(1, 1)	-18	512	512	0.03236	0.03155	0.03201	0.01446

Table 1. Parameters of the runs performed with ColDICE (Sousbie & Colombi 2016). The first column indicates the designation of the run. The second column corresponds to the relative amplitudes of the initial sine waves, namely, $\epsilon_{2D} = \epsilon_y/\epsilon_x$ and $\epsilon_{3D} = (\epsilon_y/\epsilon_x, \epsilon_z/\epsilon_x)$ for two and three sine waves, respectively. The third column gives the value of ϵ_x . The fourth and fifth columns indicate the resolutions of the numerical simulations: the spatial resolution of the grid used to solve the Poisson equation, and the spatial resolution of the mesh of vertices used to construct the initial tessellation, respectively. In the sixth column, a_{sc}^{LPT} is the shell-crossing time estimated by 40LPT for the two-sine waves initial conditions and by 15LPT for the three-sine waves initial conditions. The seventh, eighth, and ninth columns indicate the scale factor a_{sc} at shell-crossing measured in the simulations (see Appendix A1 in STC), the scale factor of the output time used for the analyses performed shortly after collapse in the simulations, and the fractional difference between a_{sc} and a_{sim} , respectively.

We will also present the normalised force $\tilde{F}(x)$ given by

$$\tilde{F}(x) = \frac{F(x)}{4\pi G a^2 \bar{\rho}}. \quad (54)$$

4.2. Force along the shell-crossing direction, F_x

Fig. 2 displays, just after shell-crossing, the x -component of the force F_x as a function of x in the vicinity of the pancake for various values of y . Perturbative order increases from left to right, while initial conditions are given, from top to bottom, by Q1D-2SIN, ANI-2SIN, Q1D-3SIN, and ANI-3SIN.

We first notice the perfect agreement between the analytical formula (51) (solid curves) and the exact solution (14) (dashed curves), which fully justifies the mathematical relevance of the formalism developed in Sect. 3. In particular, the sharp transition between the single-stream and the multi-stream region is perfectly described by Eq. (51), with the variations with y (and z , not shown here) accounted for correctly. The discontinuity observed on the derivative of the x -component of the force field is a typical signature of the presence of caustics, as found previously in the 1D case (see, e.g., Gurevich & Zybin 1995; Colombi 2015), as well as in caustic rings (see, e.g., Fig. 8 in Sikivie 1999).

Interestingly, the results do not strongly depend on the perturbation order in Fig. 2. This is because both the analytical formula (51) and the numerical calculation (14) rely on LPT displacement, which shows fast convergence behaviour with LPT order after synchronisation of shell-crossing times (see Fig. 10 in STC).

Obviously, our approach works because parameter Δ in Eq. (53) is very small, which makes the pancake quasi one dimensional, independently of the values of ϵ_{2D} and ϵ_{3D} as long as $\epsilon_y, \epsilon_z < \epsilon_x$. We will see in Sect. 4.4 how the accuracy of the description deteriorates with increasing Δ , that is with increasing time interval after collapse.

4.3. Force orthogonal to the shell-crossing direction

We now turn to the component F_y of the force orthogonal to the shell-crossing direction (hence coplanar with the pancake) inside and in the vicinity of the pancake, as shown in Fig. 3 very shortly after collapse (note that the plot of the z -component, F_z , in the 3D case, would give results very similar to F_y , so is not shown here). As already mentioned in Sect. 3.3, contrary to F_x ,

the exact gravitational force field given by Eq. (14), displayed as dashed curves, is not significantly affected by the presence of caustics, with a weak dependence on x , $F_y \propto y$ and $F_z \propto z$ close to the origin, while F_y and F_z are locally even with respect to z and y , respectively (not shown on the figures). In particular we found by comparing $F_{y,z}$ just before and after collapse ($\Delta = \pm 0.001$) that it hardly changes during this period of time. These results suggest that shell-crossing along the x -direction does not strongly affect the dynamics along other axes. This property allows us to still use the high-order LPT solution, that is the acceleration computed as the second time derivative of the LPT displacement, to describe the y and z components of the force as long as the LPT series converges, as shown by the solid curves in Fig. 3 after averaging over the streams according to Eq. (15). The solid curves in Fig. 3 converge to the exact solution when increasing perturbative order n , except that 15th order is still insufficient for ANI-3SIN. Convergence is eased when approaching quasi one dimensional initial conditions (Q1D-2SIN and Q1D-3SIN), thanks to the much faster convergence of the LPT series in this case. We also checked in Eq. (15) that the LPT accelerations computed inside each stream are nearly the same.

Another important finding is that the dashed curves are only weakly dependent on LPT order, which is a consequence of synchronisation of LPT predictions with their own collapse time. We shall see in Sect. 5 that they actually agree very well with the measurements in ColDICE simulations. As shown by STC, the density field, which stems from synchronized LPT displacements and sources the force field, is very well described by LPT predictions even of relatively low order. On the other hand, the solid curves in Fig. 3 show that the LPT acceleration converges much more slowly than the LPT displacement, even after synchronisation. This is a rather obvious consequence of the fact that time derivatives give more weight than cumulative quantities to deviations from the exact solution, since these last ones increase with time. Similarly, STC found that convergence of LPT for velocities fields was slower than for density fields. Note thus that Eq. (14) provides, at fixed LPT order, a much more accurate way to compute the gravitational acceleration than the second time derivative of the LPT displacement, as already mentioned in last paragraph of Sect. 2.2. In other words, it provides a resummation of the gravitational force that could be used to improve on LPT predictions even prior to shell crossing (i.e., even in the absence of synchronisation, see Fig. 6 in Sect. 5).

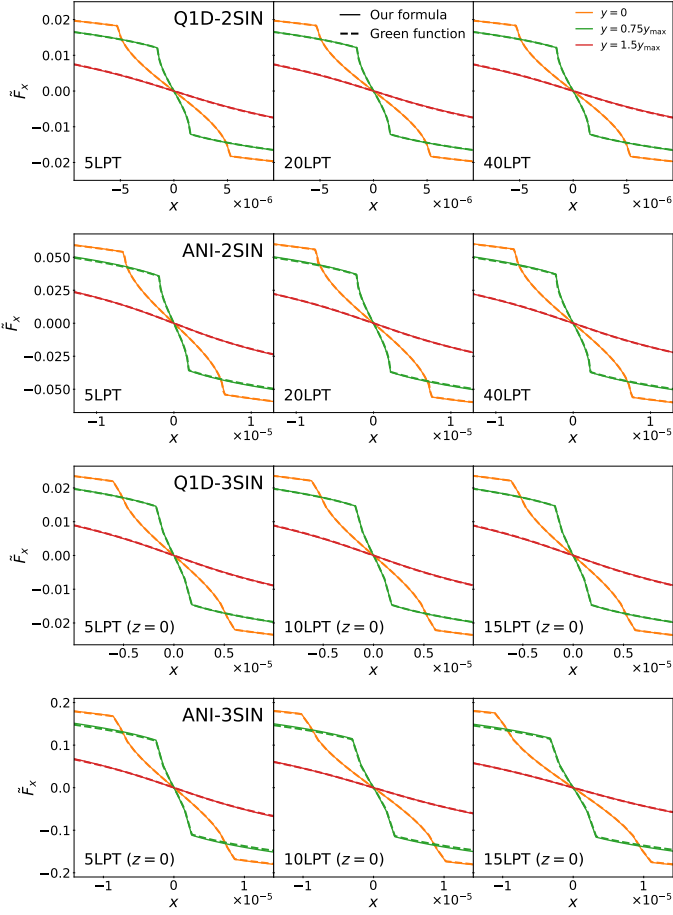


Fig. 2. x -component of force as a function of x inside and in the vicinity of a pancake seeded by three sine waves in the context of LPT dynamics, with $-1.8 \leq x/x_{\max} \leq 1.8$, where x_{\max} is the maximum extension of the caustic region along x axis as given by Eq. (44) in our approximate formalism. The output time is set to be $\Delta = 0.001$ with synchronisation (see Eq. (53)). On each panel, the curves of various colours correspond to different values of y (and $z = 0$ in the 3D case), namely $y/y_{\max} = 0$ (orange), 0.75 (green), and 1.5 (red, outside the multistream region), where y_{\max} is the maximum extension of the caustic region along y axis (Eq. 45). From top to bottom, we consider Q1D-2SIN, ANI-2SIN, Q1D-3SIN, and ANI-3SIN. From left to right, the predictions are made with 5, 20 (10), and 40LPT (15LPT) for two-sine (three-sine) waves initial conditions, respectively. The dashed and solid lines represent, respectively, the “exact” force given by Eq. (14) and the analytic prediction (51).

4.4. Time dependence

In the analyses performed in the two previous sections, we made sure that the assumptions of Sect. 3.1 were valid by taking a very small value of $\Delta = 0.001$ in Eq. (53). In Fig. 4, we now investigate how the results change when Δ increases, up to the values $\Delta_{\text{sim}}^{\text{LPT}} = \Delta_{\text{sim}}(a_{\text{sc}}/a_{\text{sc}}^{\text{LPT}})$ with Δ_{sim} listed in Table 1, that are used for measurements of Sect. 5 in ColDICE simulations.

We first focus on F_x by examining left panels of Fig. 4. As expected, the analytical prediction (51) deviates more and more from the exact solution as Δ increases. For a given value of Δ , e.g. $\Delta = 0.01$, deviations are slightly larger for ANI cases than Q1D cases, in agreement with intuition. Yet, even for non Q1D initial conditions, the local quasi one-dimensional nature of the dynamics dominates if Δ is small enough. Obviously our approach has its limits, as illustrated by bottom right panel of the left part of Fig. 4. Importantly, deviations between dashes and

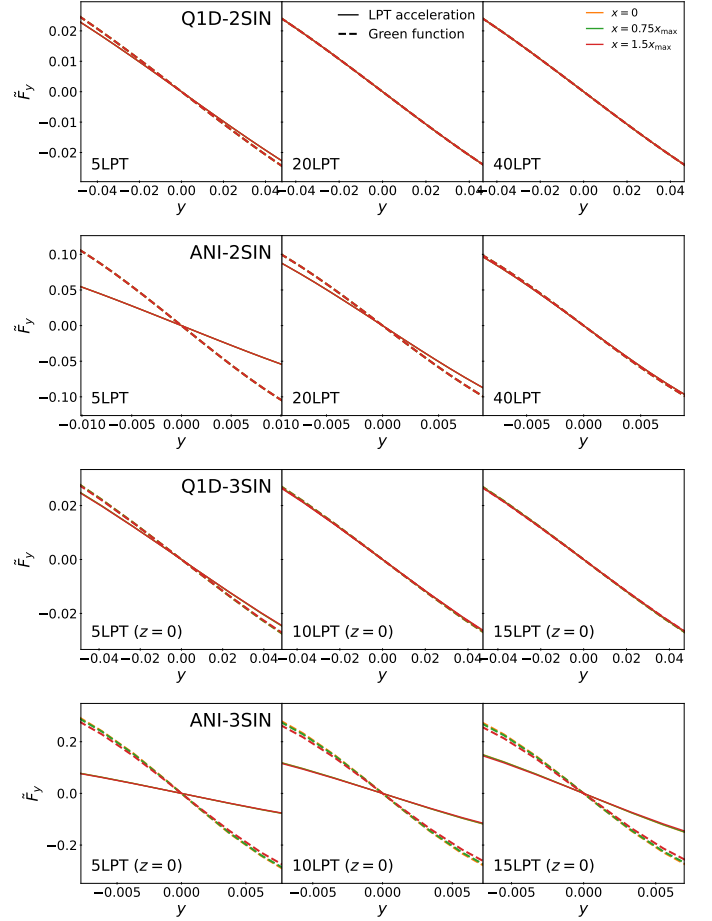


Fig. 3. Same as Fig. 2 but for the y -component of the force, F_y , in the range $-1.8 \leq y/y_{\max} \leq 1.8$ for $x/x_{\max} = 0$ (orange), 0.75 (green), and 1.5 (red). The dashed and solid lines represent, respectively, the force given in Eq. (14) and the LPT acceleration given in Eq. (15). Due to the weak dependence of F_y on the presence of the caustic and the very small range of values of x considered, the curves for $x/x_{\max} = 0, 0.75$, and 1.5 nearly perfectly overlap.

solid lines on left part of Fig. 4 are not related to performances of high order LPT but instead, to our truncation to third order of the Taylor expansion in Eqs (20)–(22), as illustrated by Fig. A.1 in Appendix A. This also explains why deviations also increase with the value of y , when passing from the green to the red curve on left panels of Fig. 4. We note that it would be possible to correct the solutions (41) of three-value problem by including perturbatively higher order terms in the Taylor expansion in \mathbf{q} , that would most certainly improve the agreement between the solid and the dashed curve in the ANI-3SIN case, even for $\Delta = 0.0289$. Of course, such a procedure cannot apply to arbitrarily large Δ . It would moreover become pointless since LPT becomes a worse prescription of the dynamics as Δ increases. Indeed LPT has a finite convergence radius in time and does not take into account the feedback of the gravitational force inside the caustics, which is the objective we have in mind when computing the force field.

Next, we focus on F_y and examine right panels of Fig. 4,⁴ which confirm what we found in previous section for $\Delta = 0.001$: except for the ANI-3SIN case, the LPT acceleration given by Eq. (15) agrees well with the exact solution (14) at all times considered. It stays pretty insensitive to the existence of the multi-

⁴ The z -coordinate of the force, not shown here, would give very similar results.

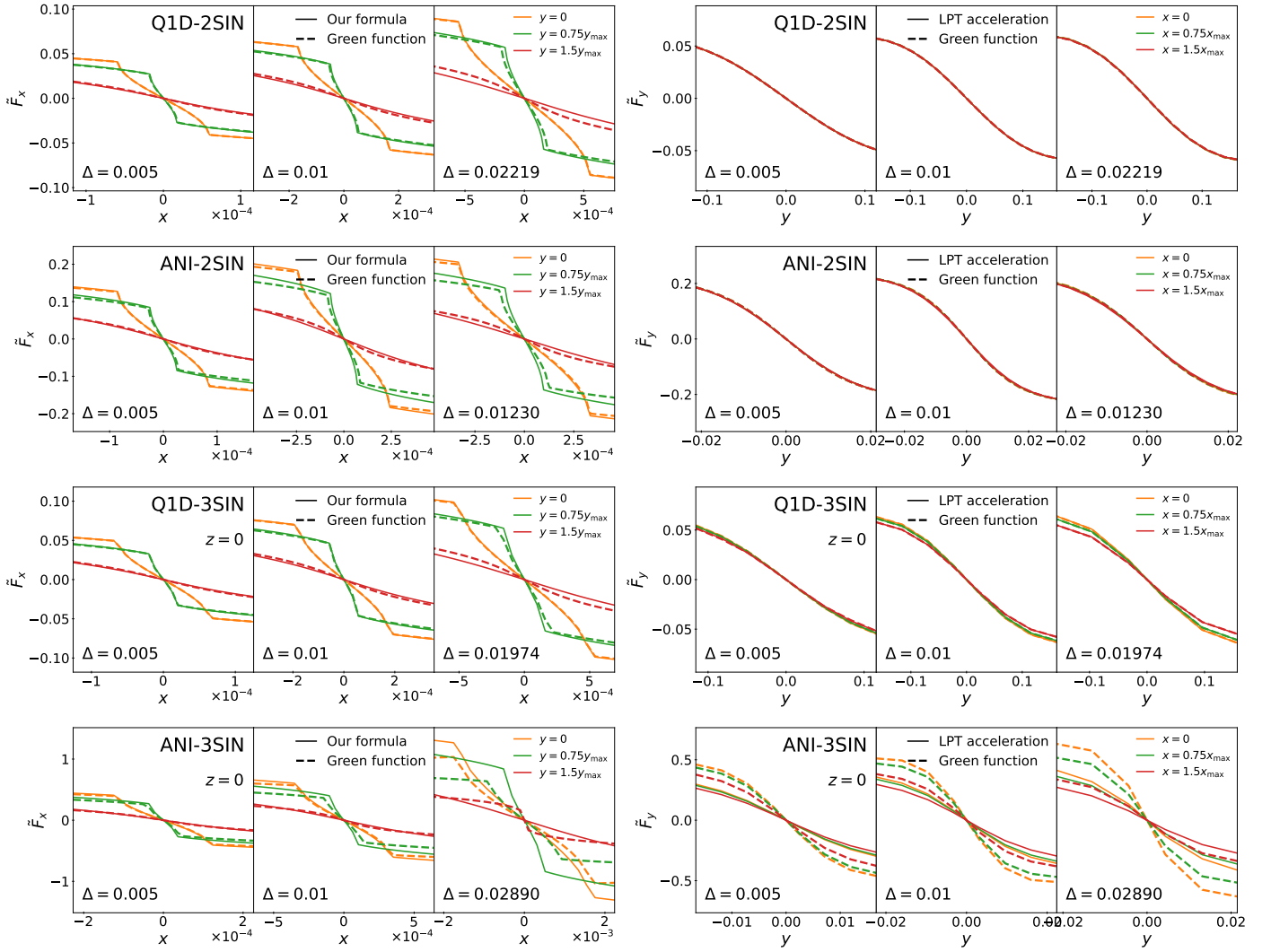


Fig. 4. Time dependence of the x - and y -components of the force, for various sine wave initial conditions considered in this article, as indicated in the panels. On each row, the output time, traced by the parameter Δ in Eq. (53), increases from left to right, as indicated on each panel, with $\Delta = \Delta_{\text{sim}} (a_{\text{sc}}/a_{\text{sc}}^{\text{LPT}})$ on the right panels, where Δ_{sim} corresponds to the output time in the simulations discussed in Sect. 5 (see also Table 1). Note that in this last case, the value indicated on the figure is not Δ but Δ_{sim} , but the differences are small. The exact solution given by Eq. (14) applied to the LPT displacement (dashes) is compared to the analytical formula (51) for F_x and with the LPT acceleration (15) for F_y (solid lines). The two top and two bottom rows use 40LPT and 15LPT respectively to compute the displacement field and its acceleration. In the to bottom rows, we assume $z = 0$.

stream region, as long as the pancake remains very thin and preserves the one dimensional nature of the local dynamics, which facilitates convergence of the LPT series. This is obviously not the case of ANI-3SIN, where F_y presents significant variations with x that increase with time, especially for the exact solution. Note that the good agreement between theory and exact solution is obviously greatly facilitated by 40LPT in 2D, while only 15LPT is used in the 3D cases. Still, although the Q1D-3SIN case uses only the 15LPT solution for the acceleration, theory and exact solutions still agree very well with each other. On the other hand, in the ANI-3SIN case, the LPT acceleration deviates significantly from the exact force given by Eq. (14) and this even before shell-crossing, while the 15LPT displacement itself remains a very good approximation of the true displacement measured in simulations, even for $\Delta = \Delta_{\text{sim}}^{\text{LPT}}$, as shown below in Sect. 5.

5. Comparison to simulations

In the previous sections, we tested the accuracy of force field calculations by using LPT as a proxy of the dynamics. We now rely on actual measurements in Vlasov-Poisson simulations to test LPT itself, since it is used for computing the coefficients in Eqs. (34)–(36) that lead to the asymptotic expression (51) as well as the gravitational acceleration as a second time derivative of the LPT displacement in Eqs. (49) and (15).

The simulations we use to conduct the analyses were performed by Colombi (2021) and STC with the public Vlasov code CoLDICE (Sousbie & Colombi 2016). This solver follows directly the evolution of a self-gravitating three-dimensional (two-dimensional) phase-space sheet in six-dimensional (four-dimensional) phase-space with an adaptive tessellation of tetrahedra (triangles). The initial configuration uses a regular pattern of n_s vertices with null velocities to construct the tessellation. At the beginning of the simulations, this pattern is perturbed by Zel'dovich motion following Eq. (52). During runtime, Poisson

equation is solved in ColDICE on a mesh of fixed resolution n_g . Table 1 indicates the values of n_s and n_g adopted for our runs, as well as the expansion factor a_{sim} of the snapshot used for the analyses slightly beyond first shell-crossing. Other technical details on the simulations we use are already provided in Colombi (2021) and STC, so we do not repeat them here. In Appendix C, we explain how we measure the force field from the tessellation.

To compare LPT predictions to measurements in simulations, we proceed as in Sect. 4 and synchronize high-order LPT solutions (here, 40LPT for the 2D case and 15LPT for the 3D case) as follows. First, LPT solutions are evolved to their own shell crossing time, designed in Table 1 by $a_{\text{sc}}^{\text{LPT}}$ (namely $a_{\text{sc}}^{(40)}$ and $a_{\text{sc}}^{(15)}$ for 2D and 3D respectively, in the notations of Sect. 4). Next, time is advanced up to expansion factor $a = a_{\text{sc}}^{\text{LPT}} + (a_{\text{sim}} - a_{\text{sc}})$, where a_{sc} and a_{sim} are respectively the shell-crossing time measured by STC in the simulations and the expansion factor of the snapshot we consider for the analyses, as listed in Table 1. Note that the output times of the simulations, which are different for each initial condition, are, in terms of relative expansion factor values, closer to the shell crossing time in the following order: ANI-2SIN, Q1D-3SIN, Q1D-2SIN and ANI-3SIN (see the last column in Table 1).

Fig. 5 compares analytical predictions to measurements in the simulations of the force field for the various sine wave initial conditions introduced in Sect. 4.1, except the axisymmetric ones which are discussed further below. The first thing to notice when examining this figure is the excellent agreement between the measurements (black dots) and the numerical solution of Poisson equation based on the Green function approach, Eq. (14), when applied to the density field sourced by the LPT displacement after synchronisation (orange dashes). This confirms the earlier investigations of STC on the density field, which compared post-collapse predictions based on the ballistic approximation, where the velocity field is frozen at collapse time, to the same simulations data. At the times considered here, the ballistic approximation should not differ much from LPT predictions pushed beyond shell-crossing as performed in the present work. Such a good agreement between LPT and simulations fully validates the conclusions of the analyses of Sect. 4. Thus, in Fig. 5, we observe the same matches/discrepancies between the solid green (left panels)/blue (right panels) curves and the black dots/orange dashes that we can discern in Fig. 4, between the solid curves and the dashes. This confirms again the validity of our theoretical predictions when two conditions are met: (i) sufficiently short period of time after collapse, so that our local Taylor expansion of the displacement field remains accurate enough to estimate the component of the force along the shell-crossing direction (orthogonal to the pancake) with Eq. (51), and (ii) sufficiently high LPT order for the LPT displacement to be accurate around shell-crossing time, as well as its second time derivative used in Eq. (15) as an approximation for the component of the force orthogonal to the direction of collapse (coplanar with the pancake). Obviously, these two conditions are not met for ANI-3SIN as already discussed in detail in Sect. 4, but are facilitated in the Q1D cases.

Interestingly, Eq. (49) (solid blue curves on left panels of Fig. 5) approximates very well the x -component of the force, except again for ANI-3SIN. Summing up correctly the LPT accelerations in the multi-stream regions using either Eq. (49) or Eq. (15) also provides, shortly after shell-crossing, a very good self-consistent approximation of all the components of the force field provided that the LPT series is converged.

The synchronisation process plays an important role in the analytical prediction of the force along the direction of shell-crossing, F_x , because collapse time changes with LPT order and the effect of shell-crossing is dramatic on F_x . However, this is not really the case for the orthogonal component –coplanar with the pancake– that preserves pretty much the single-stream behaviour of the motion, as already discussed in Sect. 4.3. We double check again this property by reproducing the right panels of Fig. 5 on Fig. 6 but without synchronisation of LPT predictions. For the 40th LPT order and the 15th LPT order respectively in 2D and 3D, we indeed distinguish no difference between the two figures. Additionally, various LPT orders are considered on Fig. 6. Interestingly, the LPT accelerations (solid lines) show slow convergence, while the forces computed with the Green function method from the LPT displacements (Eq. 14, dashed lines) show very fast convergence, even for ANI-3SIN. In other words, as mentioned in Sect. 4.3, Eq. (14) represents a *resummation* of LPT that provides a much more accurate description of the gravitational acceleration than the second time derivative of the LPT displacement. This property might turn very useful for future applications.

Before closing this section, we examine in Fig. 7 axial-symmetric initial conditions, SYM-2SIN and SYM-3SIN. In this case, shell-crossing occurs simultaneously along all the axes of the dynamics, so we expect qualitatively different behaviour from the Q1D and ANI cases. Strictly speaking axial-symmetric configurations have zero weight from the statistical point of view, but can in practice still be present at the coarse level, e.g. very high peak in random Gaussian fields which are expected to be rounder (see, e.g., Bardeen et al. 1986).

The axisymmetric case does not correspond to the superposition of 2 and 3 pancakes in the 2D and 3D cases, respectively (see Gurevich & Zybin 1995, for analytical predictions of the gravitational potential under these assumptions). Indeed, the caustic structure stemming from simultaneous shell-crossings along several directions is convoluted, as shown by STC, which translates into multiple discontinuities of the derivative of the force field along each axis. For instance, on top left panel of Fig. 7, there are four sharp transition points on the force field instead of two on top left panel of Fig. 5. Even if the analytical predictions discussed in Sect. 3 are irrelevant for SYM cases, it is still possible to use the Green function approach in Eq. (14) with the high order LPT displacement field used as a proxy for the dynamics, as indicated by the dashed curves on Fig. 7. While 40LPT successfully reproduces the post-collapse gravitational field in the 2D case, 15LPT is not accurate enough. Turning to the 3D case, 15LPT is not even good from the qualitative point of view, as already noticed for STC for the density field itself. However, SYM-3SIN is further away from shell-crossing than SYM-2SIN in terms of the parameter Δ as shown in last column of Table 1, which explains partly the worse performance of LPT predictions for SYM-3SIN compared to SYM-2SIN. Another and more obvious reason for this lies in the much higher contrasts expected in SYM-3SIN compared to SYM-2SIN, which can introduce non negligible feedback effects from the multi-stream region, even very shortly after shell-crossing, as already extensively discussed in STC.

6. Summary

In this article, we studied the gravitational force field generated by pancakes shortly after collapse. Restricting to the case where the displacement field sourcing the pancake is locally symmetric, we derived approximations for the force field combining

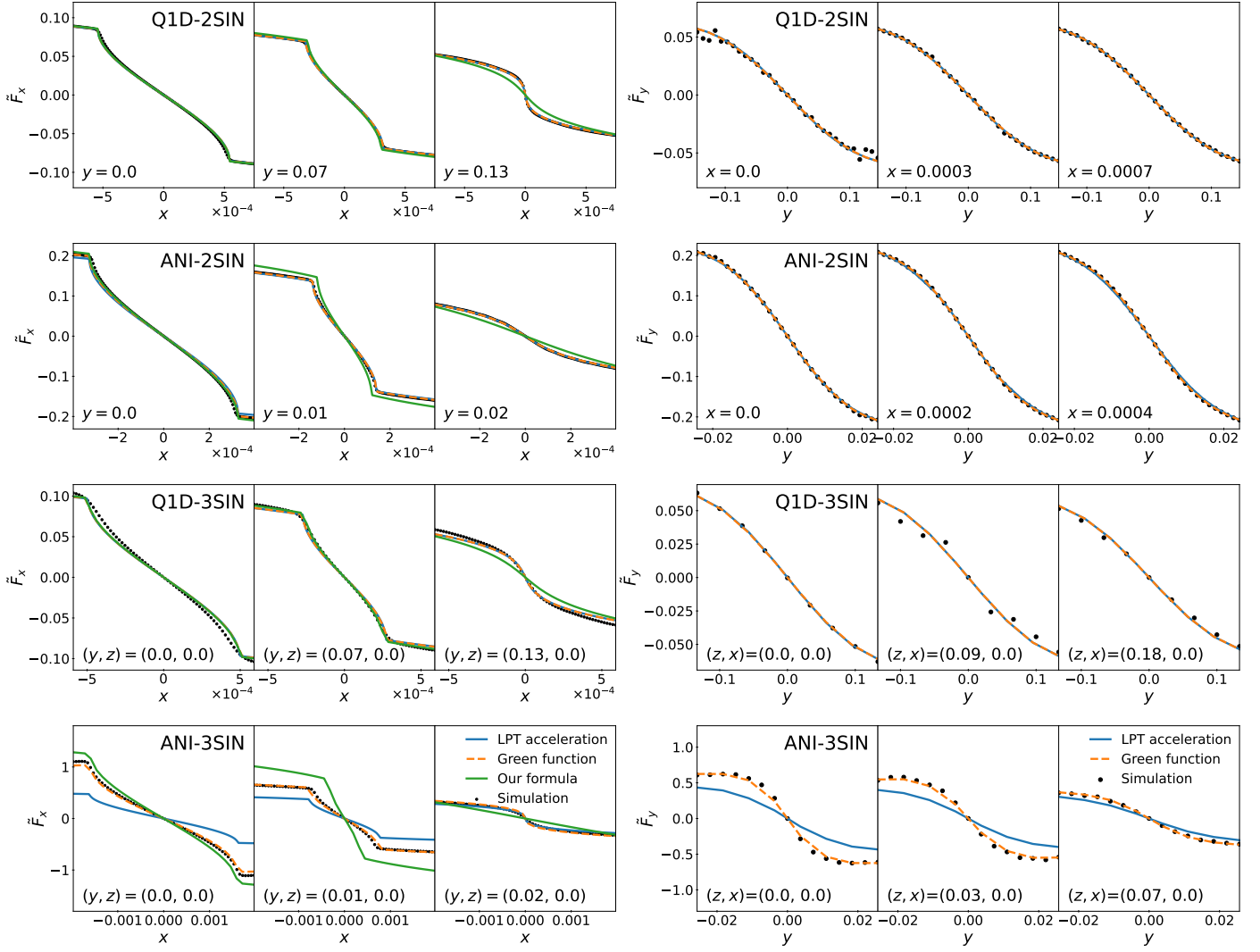


Fig. 5. Comparison between simulations and analytical predictions for F_x (left panels) and F_y (right panels) slightly beyond first shell-crossing time. From top to bottom, we consider Q1D-2SIN, ANI-2SIN, Q1D-3SIN, and ANI-3SIN initial conditions, respectively. For each initial condition, we present the force for three different values of y and/or z as indicated on each panel. The largest values of y and z are outside the multistream region. The dots stand for the measurements in the ColDICE simulations. The green solid curves on left panels give the theoretical prediction for F_x from the analytical formula (51). The solid blue lines correspond to the theoretical predictions for F_x and F_y , obtained from the LPT acceleration using Eq. (49) (only in the multi-stream region) and Eq. (15), respectively. The orange dashed lines represent the force field resulting from solving Poisson equation (14) when using the LPT displacement instead of the supposedly exact positions of particles in the ColDICE runs.

fundamentals of catastrophe theory and high order Lagrangian perturbation theory (LPT) that we carefully validated on systems seeded by two or three sine waves initial conditions. Our analyses included comparisons of theoretical predictions to measurements in Vlasov simulations performed with the public code ColDICE. The important assumption is that the time lapse after collapse, quantified here by the parameter Δ given in Eq. (53), is very short, allowing one to assume that the multistream region is locally infinitely thin. The main results of our work can be summarized as follows:

- (i) The calculation of the component F_x of the gravitational force aligned with the direction of shell-crossing (that is, orthogonal to the pancake) comes down to solving a three value problem that reduces to the resolution of a third order polynomial in the limit $\Delta \ll 1$. This process is very analogous, not surprisingly, to the 1D case, and leads to explicit expressions in terms of Eulerian coordinates, Eqs. (37), (39), (40), (41) and (51). Calculation of the various time dependent co-

efficients intervening in the expression of F_x rely on a Taylor expansion of the LPT displacement at third order in the Lagrangian position, while staying within the convergence radius of the displacement expanded as a high order series in time.

- (ii) The component F_y (and F_z) of the gravitational force orthogonal to the direction of shell-crossing (that is, in the same plane as the pancake) is rather insensitive to the presence of caustics. It can then be predicted with the usual LPT acceleration, that is the second time derivative of the LPT displacement, as long as the LPT acceleration converges as a series expansion in time. While Eq. (15) can be used to perform averaging over several streams, it is not absolutely needed. However the three value problem remains to be solved, either numerically as we did in this work, or approximately using Eqs. (37), (39), (40) and (41).
- (iii) We noted that Eq. (51) is asymptotically equivalent to Eq. (49) with the x -component of the acceleration given by

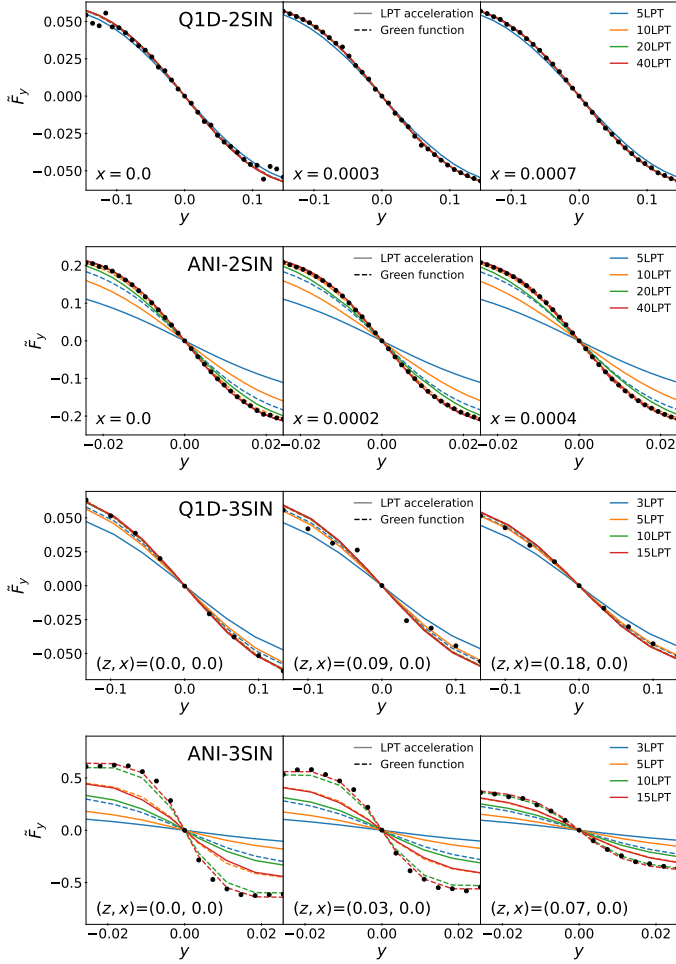


Fig. 6. Same as in the right panels of Fig. 5, but without synchronisation to collapse time at each LPT order, i.e., for a given initial condition, all the curves are calculated at the same expansion factor, a_{sim} . In addition, several LPT orders are considered as indicated on right panels, to illustrate the convergence speed.

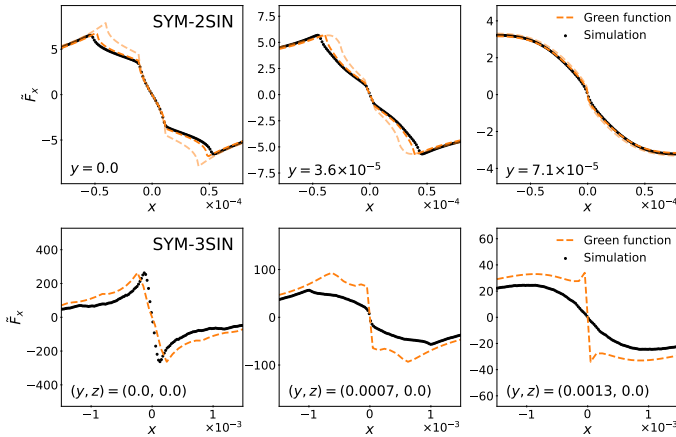


Fig. 7. Same as Fig. 5 but for the SYM-2SIN (top panels) and SYM-3SIN (bottom panels) initial conditions, except that they are no blue nor green curves, because our analytical recipes apply only to shell-crossing occurring along one direction. Only the x -component of the force is shown in Fig. 7 due to the symmetric nature of the system. In addition, the 15LPT prediction from Eq. (14) is shown as a light orange dashed curve in the 2D case.

the second time derivative of the LPT displacement, which in turn makes the approach fully consistent with (ii).

- (iv) Much higher LPT order is needed for the acceleration to converge than for the displacement, which is a natural consequence of the properties of the LPT series, of which the convergence speed decreases with successive time derivatives (see e.g., Rampf et al. 2023). However, one can solve numerically Poisson equation using the Green function approach embodied by integral Eq. (14) based on the knowledge of the LPT displacement to reach –as obvious– a convergence level as good as for the displacement. Hence Eq. (14) acts as a resummation procedure of LPT to compute accurately the gravitational field.
- (v) While quasi one-dimensional initial conditions facilitate convergence of perturbation theory predictions, our calculations apply also to pancakes seeded by peaks with a general ellipsoid shape and remain accurate as long as the pancake remains very flat, but become wrong in the extreme case where collapse takes place simultaneously along all the axes of the dynamics.

In this work, we have used LPT as an approximation of the dynamics shortly beyond collapse, but there are limitations to such an approach due to the finite radius of convergence with respect to time of the perturbative series. Another safer point of view, adopted and tested successfully by STC on our sine wave cases, consists in using a ballistic approximation, where velocities (and in the present case LPT accelerations) are frozen from collapse. While we did not adopt it here for simplicity, it would be easy to implement this ballistic approximation to compute the gravitational force field of pancakes, instead of the procedure described in points (i) and (ii) above. The advantage of the ballistic approach is to overcome the problem of LPT convergence which is known to be guaranteed in practice up to collapse (see, e.g., Rampf & Hahn 2021, STC).

The calculations presented in this work can in principle be generalised to an arbitrary (smooth and non degenerate) displacement field. Clearly, the case of a displacement field deriving from a potential in Lagrangian space (i.e. vorticity free in Lagrangian space) can be treated easily. While not fully representative of the exact dynamics since zero vorticity prior to shell-crossing is only expected in Eulerian space, a vorticity free displacement in Lagrangian space remains a very good approximation up to second order in the LPT framework, that includes Zel’dovich approximation. In the case of a displacement field deriving from a potential, it is easy to realize with the proper combination of affine transformations both in Lagrangian and Eulerian space, that one can obtain equations similar to Eqs. (34)–(36), but with additional $q_x^2 q_y$, $q_x^2 q_z$, q_y^3 and q_z^3 terms in the right member of Eq. (34), which makes solving the three-value problem and the force field calculation slightly more involved. We postpone more general analyses which do not impose the local symmetries (17)–(19) to future work.

The calculation of the force field generated in the vicinity of a protopanck represents the first step for an accurate treatment of the dynamics in the multi-stream regime, by computing corrections to the motion inside the pancakes due to the force back-reaction from the multistream regions, extending thereby the 1D calculations of Colombi (2015); Taruya & Colombi (2017); Rampf et al. (2021) to the 3D case. Of course, this approach remains limited, as it is expected to work only shortly after shell-crossing, even though it might be possible to combine it with an adaptive smoothing procedure to accurately predict large-scale structure statistics such as the power spectrum, even in the non-linear regime (see, e.g., Taruya & Colombi 2017; Halle et al.

2020, for the 1D case). Shell-crossing can also locally take place along other axes of the dynamics, leading to the formation of protofilaments and protohaloes. This is also followed by violent relaxation, that is quick folding of the phase-space sheet in multiple directions. Understanding in details the early evolution of protopanckes remains crucial to understand how multiflow dynamics is initiated and how this affects the early evolution of the statistics of the large scale matter distribution.

Acknowledgements

We thank C. Rampf for reading and commenting on the draft. SS is supported by JSPS Overseas Research Fellowships. This work was supported in part by MEXT/JSPS KAKENHI Grant Numbers JP20H05861 and JP21H01081 (AT), ANR grant ANR-13-MONU-0003 (SC), as well as Programme National Cosmology et Galaxies (PNCG) of CNRS/INSU with INP and IN2P3, co-funded by CEA and CNES (SC). Numerical computation with CoLDICE was carried out using the HPC resources of CINES (Occigen supercomputer) under the GENCI allocations c2016047568, 2017-A0040407568 and 2018-A0040407568. Post-treatment of CoLDICE data were performed on HORIZON cluster of Institut d’Astrophysique de Paris.

References

Abramowitz, M. & Stegun, I. A. 1972, *Handbook of Mathematical Functions*
 Alard, C. 2013, *MNRAS*, 428, 340
 Angulo, R. E., Hahn, O., Ludlow, A. D., & Bonoli, S. 2017, *MNRAS*, 471, 4687
 Arnold, V. I., Shandarin, S. F., & Zeldovich, I. B. 1982, *Geophysical and Astrophysical Fluid Dynamics*, 20, 111
 Baldauf, T., Mercolli, L., & Zaldarriaga, M. 2015, *Phys. Rev. D*, 92, 123007
 Bardeen, J. M., Bond, J. R., Kaiser, N., & Szalay, A. S. 1986, *ApJ*, 304, 15
 Baumann, D., Nicolis, A., Senatore, L., & Zaldarriaga, M. 2012, *J. Cosmology Astropart. Phys.*, 2012, 051
 Bernardeau, F. 1994, *ApJ*, 427, 51
 Bernardeau, F., Colombi, S., Gaztañaga, E., & Scoccimarro, R. 2002, *Phys. Rep.*, 367, 1
 Bernardeau, F., Crocce, M., & Scoccimarro, R. 2008, *Phys. Rev. D*, 78, 103521
 Bernardeau, F., Crocce, M., & Scoccimarro, R. 2012, *Phys. Rev. D*, 85, 123519
 Bernardeau, F., Taruya, A., & Nishimichi, T. 2014, *Phys. Rev. D*, 89, 023502
 Bertschinger, E. 1985, *ApJS*, 58, 39
 Beutler, F., Seo, H.-J., Saito, S., et al. 2017, *MNRAS*, 466, 2242
 Blake, C., Brough, S., Colless, M., et al. 2011, *MNRAS*, 415, 2876
 Blas, D., Garny, M., & Konstandin, T. 2014, *J. Cosmology Astropart. Phys.*, 2014, 010
 Blumenthal, G. R., Faber, S. M., Primack, J. R., & Rees, M. J. 1984, *Nature*, 311, 517
 Bouchet, F. R., Colombi, S., Hivon, E., & Juszkiewicz, R. 1995, *A&A*, 296, 575
 Bouchet, F. R., Juszkiewicz, R., Colombi, S., & Pellat, R. 1992, *ApJ*, 394, L5
 Buchert, T. 1992, *MNRAS*, 254, 729
 Buchert, T. & Ehlers, J. 1993, *MNRAS*, 264, 375
 Carrasco, J. J. M., Hertzberg, M. P., & Senatore, L. 2012, *Journal of High Energy Physics*, 2012, 82
 Carron, J. & Szapudi, I. 2013, *MNRAS*, 432, 3161
 Chakrabarty, S. S. & Sikivie, P. 2018, *Phys. Rev. D*, 98, 103009
 Colombi, S. 2015, *MNRAS*, 446, 2902
 Colombi, S. 2021, *A&A*, 647, A66
 Crocce, M. & Scoccimarro, R. 2006, *Phys. Rev. D*, 73, 063520
 Crocce, M. & Scoccimarro, R. 2008, *Phys. Rev. D*, 77, 023533
 d’Amico, G., Gleyzes, J., Kokron, N., et al. 2020, *J. Cosmology Astropart. Phys.*, 2020, 005
 Delos, M. S., Erickcek, A. L., Bailey, A. P., & Alvarez, M. A. 2018a, *Phys. Rev. D*, 97, 041303
 Delos, M. S., Erickcek, A. L., Bailey, A. P., & Alvarez, M. A. 2018b, *Phys. Rev. D*, 98, 063527
 Delos, M. S. & White, S. D. M. 2022, *arXiv e-prints*, arXiv:2209.11237
 Delos, M. S. & White, S. D. M. 2023, *MNRAS*, 518, 3509
 Diemand, J., Moore, B., & Stadel, J. 2005, *Nature*, 433, 389
 Duffy, L. D. & Sikivie, P. 2008, *Phys. Rev. D*, 78, 063508
 Feldbrugge, J., van de Weygaert, R., Hidding, J., & Feldbrugge, J. 2018, *J. Cosmology Astropart. Phys.*, 2018, 027

Fillmore, J. A. & Goldreich, P. 1984, *ApJ*, 281, 1
 Garny, M., Laxhuber, D., & Scoccimarro, R. 2023a, *Phys. Rev. D*, 107, 063539
 Garny, M., Laxhuber, D., & Scoccimarro, R. 2023b, *Phys. Rev. D*, 107, 063540
 Gouda, N. & Nakamura, T. 1988, *Progress of Theoretical Physics*, 79, 765
 Gurevich, A. V. & Zybin, K. P. 1995, *Physics-Uspekhi*, 38, 687
 Halle, A., Nishimichi, T., Taruya, A., Colombi, S., & Bernardeau, F. 2020, *MNRAS*, 499, 1769
 Henriksen, R. N. & Widrow, L. M. 1995, *MNRAS*, 276, 679
 Hernquist, L., Bouchet, F. R., & Suto, Y. 1991, *ApJS*, 75, 231
 Hertzberg, M. P. 2014, *Phys. Rev. D*, 89, 043521
 Hidding, J., Shandarin, S. F., & van de Weygaert, R. 2014, *MNRAS*, 437, 3442
 Hjorth, J. & Williams, L. L. R. 2010, *ApJ*, 722, 851
 Ishiyama, T. 2014, *ApJ*, 788, 27
 Ivanov, M. M., Simonović, M., & Zaldarriaga, M. 2020, *J. Cosmology Astropart. Phys.*, 2020, 042
 Lynden-Bell, D. 1967, *MNRAS*, 136, 101
 Matsubara, T. 2008, *Phys. Rev. D*, 77, 063530
 Matsubara, T. 2011, *Phys. Rev. D*, 83, 083518
 Matsubara, T. 2015, *Phys. Rev. D*, 92, 023534
 Melott, A. L. & Shandarin, S. F. 1989, *ApJ*, 343, 26
 Moutarde, F., Alimi, J. M., Bouchet, F. R., & Pellat, R. 1995, *ApJ*, 441, 10
 Moutarde, F., Alimi, J. M., Bouchet, F. R., Pellat, R., & Ramani, A. 1991, *ApJ*, 382, 377
 Natarajan, A. & Sikivie, P. 2006, *Phys. Rev. D*, 73, 023510
 Natarajan, A. & Sikivie, P. 2007, *Phys. Rev. D*, 76, 023505
 Navarro, J. F., Frenk, C. S., & White, S. D. M. 1996, *ApJ*, 462, 563
 Navarro, J. F., Frenk, C. S., & White, S. D. M. 1997, *ApJ*, 490, 493
 Nishimichi, T., Bernardeau, F., & Taruya, A. 2016, *Physics Letters B*, 762, 247
 Novikov, E. A. 1969, *Soviet Journal of Experimental and Theoretical Physics*, 30, 512
 Ogiya, G. & Hahn, O. 2018, *MNRAS*, 473, 4339
 Onemli, V. & Sikivie, P. 2009, *Physics Letters B*, 675, 279
 Peebles, P. J. E. 1980, *The large-scale structure of the universe*
 Peebles, P. J. E. 1982, *ApJ*, 263, L1
 Peebles, P. J. E. 1984, *ApJ*, 277, 470
 Pietroni, M. 2008, *J. Cosmology Astropart. Phys.*, 2008, 036
 Pontzen, A. & Governato, F. 2013, *MNRAS*, 430, 121
 Rampf, C. 2012, *J. Cosmology Astropart. Phys.*, 2012, 004
 Rampf, C. 2019, *MNRAS*, 484, 5223
 Rampf, C. 2021, *Rev. Mod. Plasma Phys.*, 5, 10
 Rampf, C. & Frisch, U. 2017, *MNRAS*, 471, 671
 Rampf, C., Frisch, U., & Hahn, O. 2021, *MNRAS*, 505, L90
 Rampf, C., Frisch, U., & Hahn, O. 2022, *Physical Review Fluids*, 7, 104610
 Rampf, C. & Hahn, O. 2021, *MNRAS*, 501, L71
 Rampf, C., Saga, S., Taruya, A., & Colombi, S. 2023, *arXiv e-prints*, arXiv:2303.12832
 Rampf, C., Villone, B., & Frisch, U. 2015, *MNRAS*, 452, 1421
 Saga, S., Taruya, A., & Colombi, S. 2018, *Phys. Rev. Lett.*, 121, 241302
 Saga, S., Taruya, A., & Colombi, S. 2022, *A&A*, 664, A3 (STC)
 Shandarin, S. F. & Zeldovich, Y. B. 1989, *Reviews of Modern Physics*, 61, 185
 Sikivie, P. 1998, *Physics Letters B*, 432, 139
 Sikivie, P. 1999, *Phys. Rev. D*, 60, 063501
 Sikivie, P., Tkachev, I. I., & Wang, Y. 1997, *Phys. Rev. D*, 56, 1863
 Sousbie, T. & Colombi, S. 2016, *Journal of Computational Physics*, 321, 644
 Tam, H. 2012, *arXiv e-prints*, arXiv:1205.1260
 Taruya, A., Bernardeau, F., Nishimichi, T., & Codis, S. 2012, *Phys. Rev. D*, 86, 103528
 Taruya, A. & Colombi, S. 2017, *MNRAS*, 470, 4858
 Taruya, A. & Hiramatsu, T. 2008, *ApJ*, 674, 617
 Taruya, A., Nishimichi, T., Saito, S., & Hiramatsu, T. 2009, *Phys. Rev. D*, 80, 123503
 Tröster, T., Sánchez, A. G., Asgari, M., et al. 2020, *A&A*, 633, L10
 Valageas, P. 2007, *A&A*, 465, 725
 Valageas, P., Nishimichi, T., & Taruya, A. 2013, *Phys. Rev. D*, 87, 083522
 White, S. D. M. 2022, *MNRAS*, 517, L46
 Yano, T. & Gouda, N. 1998, *ApJS*, 118, 267
 Yano, T., Koyama, H., Buchert, T., & Gouda, N. 2004, *ApJS*, 151, 185
 Zel’dovich, Y. B. 1970, *A&A*, 5, 84
 Zhao, G.-B., Wang, Y., Saito, S., et al. 2019, *MNRAS*, 482, 3497
 Zheligovsky, V. & Frisch, U. 2014, *Journal of Fluid Mechanics*, 749, 404
 Zukin, P. & Bertschinger, E. 2010a, *Phys. Rev. D*, 82, 104044
 Zukin, P. & Bertschinger, E. 2010b, *Phys. Rev. D*, 82, 104045

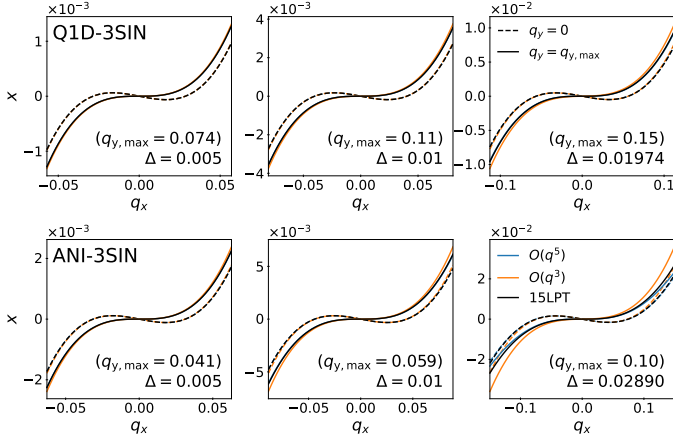


Fig. A.1. x coordinate as a function of q_x for Q1D-3SIN (top panels) and ANI-3SIN (bottom panels) initial conditions at various output times, with $\Delta = 0.005$ (left), 0.01 (centre), and $\Delta_{\text{sim}} = a_{\text{sim}}/a_{\text{sc}} - 1$ as given in right column Table 1 (right). The solid and dashed curves correspond to $q_y = 0$ and $q_y \approx q_y^{\text{max}}$, where q_y^{max} is the the max extension of the caustic in Lagrangian space along q_y axis, while $q_z = 0$. We present the results predicted by the pure 15LPT solution (black) and its Taylor expansion expression in the Lagrangian coordinate up to up to $O(q^3)$ (orange) and up to $O(q^5)$ (blue).

Appendix A: Series expansion of the displacement field

In Sect. 3.1, we derived an analytical expression for computing the x -component of gravitational force, starting from the Taylor expansion of the displacement field with respect to the Lagrangian coordinate up to third order in \mathbf{q} , given in Eqs. (23)–(25). Fig. A.1 tests the accuracy of Eqs. (23)–(25) in q_x - x space for our non-axisymmetric three-sine wave setups. Clearly, at the dynamical times considered in this paper, a third order approximation for the displacement field is sufficient in the Q1D case, but significant deviations can be noticed on bottom right panel of the figure. As expected, these deviations increase when moving away from the origin of coordinates, hence with increasing, $|x|$, $|y|$ (and $|z|$ in 3D). They explain, at least partly, the discrepancies between theory and exact solution in Fig. 4. Another significant source of error is the approximation of y and z coordinates at linear order in \mathbf{q} (Eqs. 35 and 36), that we do not examine here. Note that, as long as higher order corrections remain small, it would be possible to correct perturbatively the three-value solution derived from the third order Taylor expansion to include higher order contributions. Here, we notice that 5th order already brings very significant improvements, even if we should also check what happens in other planes.

Appendix B: Calculation of the force: truncation of integral (14)

Throughout this article, we compare our analytical predictions for the force to direct calculations of the integral (14) over a finite interval, $[-q_{\text{max}}, q_{\text{max}}]$. Our systems seeded by sine wave initial conditions are periodic, hence the problem comes down to compute the gravitational contribution of each matter element inside the simulation volume of size L , plus all the periodic replica. Many techniques exist in the literature to perform such a calculation quickly, for instance Ewald summation (see, e.g. Hernquist et al. 1991). Our brute force technique allows us to have rather accurate estimates of pairwise interactions between closely ele-

ments of mass, which is necessary given the very thin nature of the caustic structures, but fails to account for the contribution of all remote elements, including replica, which can make the force field calculation inaccurate.

To validate the choice of our somewhat simplistic technique, Fig. B.1 presents the x - (top panels) and y -components (bottom panels) of the force for our (non axisymmetric) sine wave initial conditions, restricting to the local neighbourhood of the pancake. All the output times are the same as in Fig. 5, which compares analytical predictions to simulations. We see that the x -component of the force at the scales of interest is dominated by the influence of the caustics and is thus quite insensitive to the replica given these small values of x , so a truncation of the integral (14) at $q_{\text{max}} = L/2$ is enough for all the initial conditions (including SYM-2SIN and SYM-3SIN, not shown in Fig. 5). On the other hand, the y -component of the force can be significantly affected by the replicas for Q1D initial conditions, but from lower panels of Fig. 5, $q_{\text{max}} = 5L/2$ seems sufficient for adequate convergence of the integral (14). In practice, we adopted the values listed in Table C.1 for the measurements in the CoLDICE simulations, and $q_{\text{max}} = L/2$ for F_x , $q_{\text{max}} = 20L/2$ for $F_{y,z}$, for other calculations using the LPT displacement in Eq. (14).

Appendix C: Force measurement in simulations

In CoLDICE, the dark matter distribution is represented with an adaptive tessellation of simplices, that is an ensemble of connected triangles and tetrahedra, respectively in two and three dimensions. To compute the force field $\tilde{\mathbf{F}}(\mathbf{x})$ at a given point of space, we employ a direct approach consisting in replacing each simplex with a set of particles. To do so, if needed, each simplex is refined isotropically ℓ_{max} times. At the end, each sub-simplex is replaced with a single particle lying at the barycentre of the its vertices. For best accuracy, the refinement process exploits the quadratic nature of each simplex thanks to additional tracers used in CoLDICE. To avoid divergences due to the singular nature of the force field induced by a point particle distribution, we introduce additional softening as follows:

$$\tilde{\mathbf{F}}(\mathbf{x}) = \frac{m}{2^{d-2} \times 2\pi} \frac{\mathbf{x} - \mathbf{x}_0}{(|\mathbf{x} - \mathbf{x}_0|^2 + \varepsilon^2)^{d/2}}, \quad (\text{C.1})$$

where, $d = 2$ or 3 is the dimension of space, m and \mathbf{x}_0 are respectively the (normalised) mass and the position of the particle. This equation does not account for the background correction proportional to \mathbf{x} in equation (14), that has to be added at the end of the calculation. Depending on the coordinate of the force field considered, a set of periodic replica of each particle with positions

$$\mathbf{x}_0 + (i, j, k) L, \quad (\text{C.2})$$

can contribute, with integers $i, j, k \in [-n_{\text{rep}}, n_{\text{rep}}]$, which is equivalent to restrict the integral (14) to the interval $[-q_{\text{max}}, q_{\text{max}}]$, with $q_{\text{max}} = (n_{\text{rep}} + 1/2)L$. The values of q_{max} we adopted are listed in Table C.1. They are large enough according to the convergence tests discussed in Appendix B.

Because we examine the system just after shell-crossing, it is important to have an accurate description of the phase-space sheet inside a region containing the caustics. This region is chosen to be a thin rectangular parallelepiped covering the intervals $x \in [-x_{\text{max}}, x_{\text{max}}]$, $y \in [-y_{\text{max}}, y_{\text{max}}]$ and $z \in [-z_{\text{max}}, z_{\text{max}}]$ (the latter in 3D only) in each dimension. Outside this region, each simplex is replaced with a single particle and inside it, each simplex is adaptively refined $\ell_{\text{max}} \geq 1$ times, with a value of ℓ_{max} depending on initial conditions.

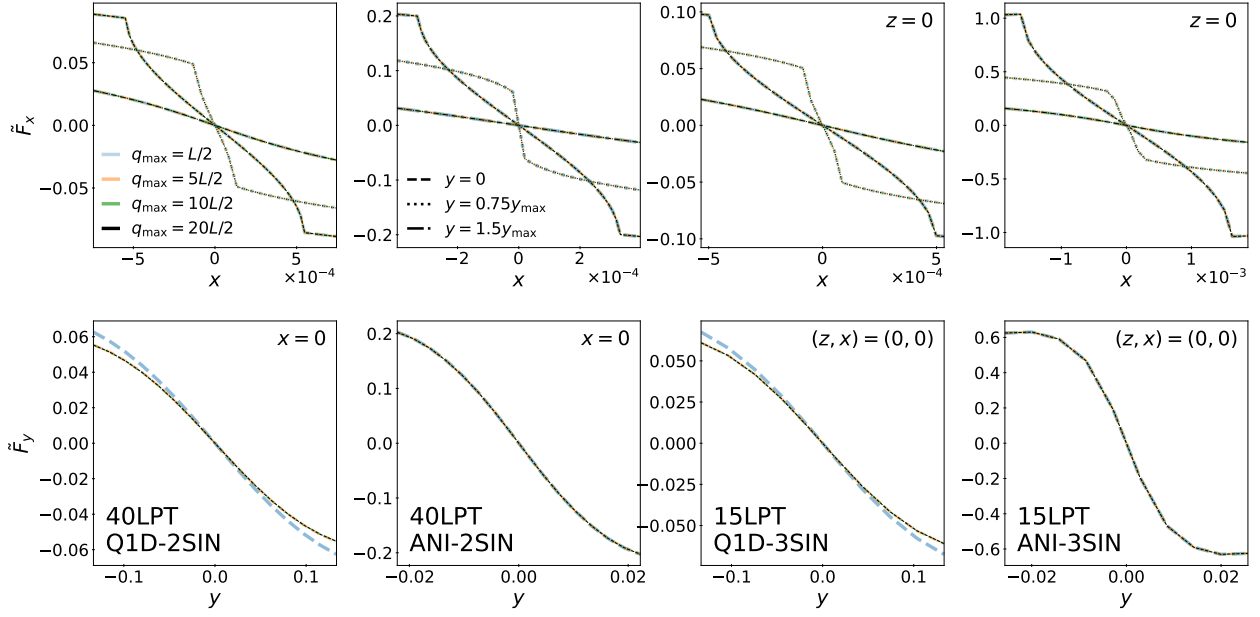


Fig. B.1. Tests of the choice of the bounds of integral (14). The x and y coordinates of the force are plotted, respectively, on top and bottom panels, for various choices of the integration range $[-q_{\max}, q_{\max}]$ with q_{\max} ranging from $L/2$ to $20L/2$ as indicated on upper left panel. From left to right, we consider Q1D-2SIN, ANI-2SIN, Q1D-3SIN, and ANI-3SIN initial conditions. On top panels, various values of y are considered as indicated on second panel of the top row, while the bottom panels only assume $x = 0$ since other values of x would not differ significantly. We also set $z = 0$ in the three-dimensional cases considered in two top-right and two bottom-right panels. Note that the output time chosen in this figure is the same as in Fig. 5. We see that all the curves corresponding to different values of q_{\max} are superimposed on each other, except for $q_{\max} = L/2$ for the Q1D cases.

Designation	q_{\max}	x_{\max}	y_{\max}	z_{\max}	ℓ_{\max}	ε
<i>Quasi 1D</i>						
Q1D-2SIN	$L/2$ for F_x , $30.5L$ otherwise	0.00075	0.15		2	1.1718750×10^{-5}
Q1D-3SIN	$L/2$ for F_x , $5L/2$ otherwise	0.0006	0.15	0.20	4	9.375×10^{-6}
<i>Anisotropic</i>						
ANI-2SIN	$L/2$ for F_x , $30.5L$ otherwise	0.0004	0.025		2	6.25×10^{-6}
ANI-3SIN	$L/2$ for F_x , $7L/2$ otherwise	0.002	0.0275	0.07	2 for $q_{\max} = L/2$ 1 for $q_{\max} = 7L/2$	3.125×10^{-5}
<i>Axial-symmetric</i>						
SYM-2SIN	$L/2$	0.00008	0.00008		2	1.25×10^{-6}
SYM-3SIN	$L/2$	0.0015	0.0015	0.0015	0	2.34375×10^{-5}

Table C.1. Parameters intervening in the measurement of the force field in the Vlasov simulations as described in Appendix C. From left to right: designation of the run, truncation parameter q_{\max} , coordinates x_{\max} , y_{\max} and z_{\max} of the upper right corner of the rectangular region where higher sampling of simplices is performed using ℓ_{\max} successive refinements as indicated in the next column; finally, ε is the softening parameter of the force field (Eq. C.1).

The various parameters introduced in this appendix are listed in Table C.1, which completes Table 1 of the main text. Note for instance that $\varepsilon = x_{\max}/64$. Because of the high mass resolution of the 2D simulations ($n_s = 2048$), it was enough to take $\ell_{\max} = 2$ for Q1D-2SIN, ANI-2SIN and SYM-2SIN. Furthermore, due to the lower cost of the force calculation in 2D, many periodic replicas could be used, $n_{\text{rep}} = 30$. On the other hand, the 3D case is much more involved computationally, which imposes us to adopt a much smaller value of n_{rep} , yet still large enough according to the tests performed in Appendix B. The most delicate case was Q1D-3SIN, where $\ell_{\max} = 4$ was necessary to have (barely) sufficiently accurate measurements of the force field. There are two reasons for this. First, in this simulation, the initial tessellation has a lower number of simplices, $6 \times n_s^3$, with $n_s = 256$, compared to $n_s = 512$ for ANI-3SIN

and SYM-3SIN, which already imposes at least one additional refinement level in Q1D-3SIN compared to the two other cases. Second, the discrete nature of the sampling of the phase-space sheet we adopted can introduce systematic biases on the force field, which are stronger in Q1D settings due to the fact that particles, that initially form a regular mesh, tend to cluster together much more along the x direction inside and in the vicinity of the caustics than in orthogonal direction(s). This induces artificial fluctuations on the force field, especially on axes orthogonal to x (see e.g. middle panel of the right group in third row of Fig. 5), that would not appear with a proper, smooth representation of the phase-space sheet. While it would be possible (but not trivial) to implement a more optimal calculation of the force field, we did not find it necessary for our analyses.